iScience

CellPress
OPEN ACCESS

Article

Adhesion G protein-coupled receptor VLGR1/ADGRV1 regulates cell spreading and migration by mechanosensing at focal adhesions

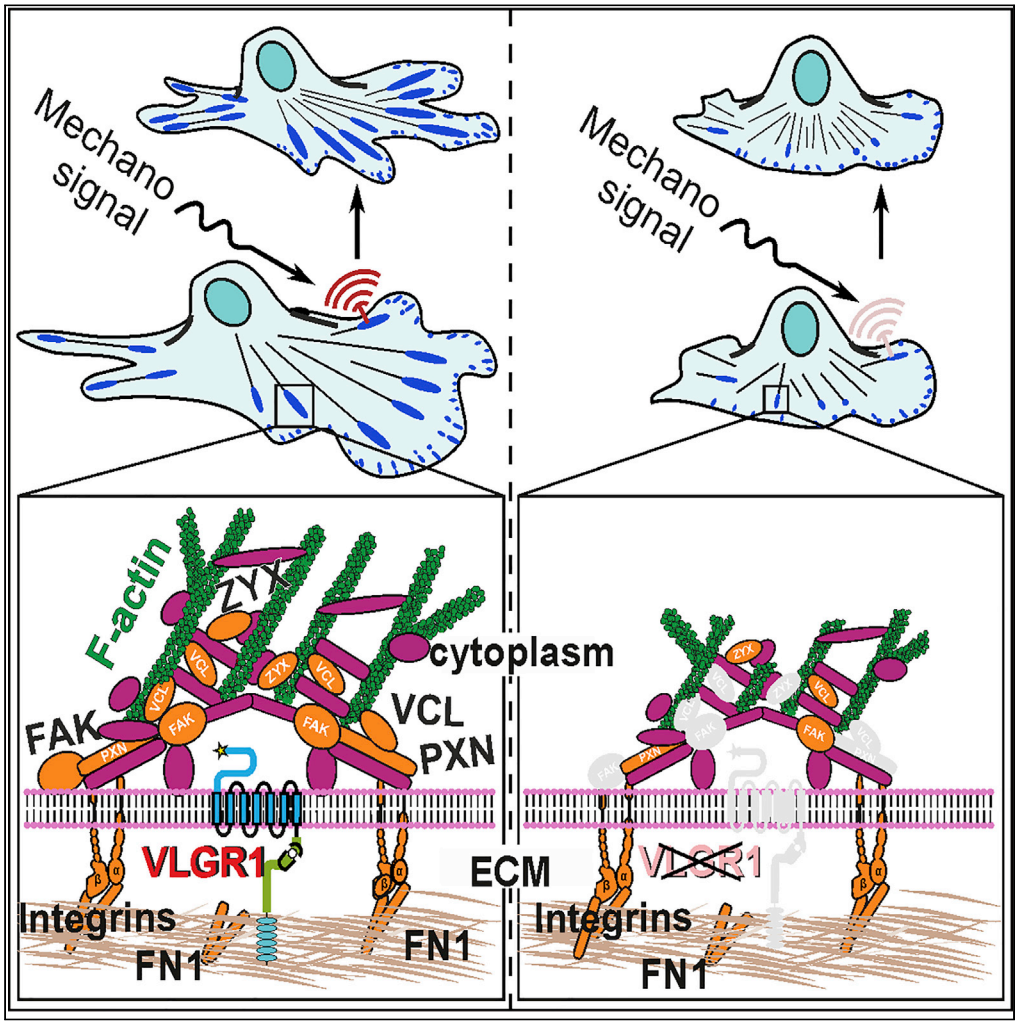

Deva K. Kusuluri, Baran E. Güler, Barbara Knapp, ..., Marius Ueffing, Gabriela Aust, Uwe Wolfrum

wolfrum@uni-mainz.de

Highlights

VLGR1 is an integral part of focal adhesions and crucial for their assembly

Absence of VLGR1 from focal adhesions alters cell spreading and cell migration

VLGR1 is a metabotropic mechanosensor in focal adhesions

Kusuluri et al., iScience 24, 102283
April 23, 2021
https://doi.org/10.1016/j.isci.2021.102283

iScience

CellPress
OPEN ACCESS

Article

Adhesion G protein-coupled receptor VLGR1/ADGRV1 regulates cell spreading and migration by mechanosensing at focal adhesions

Deva K. Kusuluri,[1] Baran E. Güler,[1] Barbara Knapp,[1] Nicola Horn,[2] Karsten Boldt,[2] Marius Ueffing,[2] Gabriela Aust,[3] and Uwe Wolfrum[1,4,*]

SUMMARY

VLGR1 (very large G protein-coupled receptor-1) is by far the largest adhesion G protein-coupled receptor in humans. Homozygous pathologic variants of *VLGR1* cause hereditary deaf blindness in Usher syndrome 2C and haploinsufficiency of *VLGR1* is associated with epilepsy. However, its molecular function remains elusive. Herein, we used affinity proteomics to identify many components of focal adhesions (FAs) in the VLGR1 interactome. VLGR1 is localized in FAs and assembles in FA protein complexes *in situ*. Depletion or loss of VLGR1 decreases the number and length of FAs in hTERT-RPE1 cells and in astrocytes of *Vlgr1* mutant mice. VLGR1 depletion reduces cell spread and migration kinetics as well as the response to mechanical stretch characterizing VLGR1 as a metabotropic mechanosensor in FAs. Our data reveal a critical role of VLGR1 in the FA function and enlighten potential pathomechanisms in diseases related to VLGR1.

INTRODUCTION

Adhesion G protein-coupled receptors (ADGRs), a unique class of the superfamily of G protein-coupled receptors (GPCRs), have been insufficiently characterized (Langenhan et al., 2016; Langenhan, 2020). Recent findings on G protein coupling, the activation mechanism by a tethered agonist (Liebscher et al., 2014), and identification of interaction partners by affinity proteomics (Knapp et al., 2019) and of their function as metabotropic mechanosensors (Scholz et al., 2015) provided prospective insights into the molecular and physiologic function of ADGRs in general (Langenhan, 2020). In the last decade, diverse physiological roles of ADGRs have been described. Several ADGRs are involved in developmental, neural, cardiovascular, immune, and endocrine processes (Knierim et al., 2019).

VLGR1 (very large G protein-coupled receptor-1)/ADGRV1, also known as GPR98 or MASS1 (monogenic audiogenic seizure susceptible-1), is by far the largest GPCR (McMillan and White, 2010). VLGR1 comprises an extremely long extracellular domain (ECD), which includes Calx-β motifs, an epilepsy-associated repeat domain, and a pentraxin domain; VLGR1 also contains the characteristic 7-transmembrane domain (7TM) and a short cytoplasmic intracellular domain (ICD) with a C-terminal PDZ (Post-synaptic density 95, Discs large, Zonula occludens-1) domain-binding motif (PBM). The ECD contains the characteristic GPCR autoproteolysis-inducing (GAIN) domain with the GPCR proteolytic site (GPS). Like other ADGRs, autocleavage at this GPS separates VLGR1 into a C-terminal fragment (CTF) and N-terminal fragment (NTF) (Hu et al., 2014). We recently found that the first 11 amino acids in the N-terminus of the CTF function as a tethered agonist that can trigger receptor activation (Knapp, et al., unpublished data). VLGR1 preferentially couples to the $G\alpha_i$ signaling pathway (Hu et al., 2014).

Several homozygous pathologic variants of the *VLGR1/ADGRV1* gene cause USH2C, a subtype of the human Usher syndrome (USH), the most common form of hereditary deaf blindness (Weston et al., 2004). Haploinsufficiency of *VLGR1/ADGRV1* associates with audiogenic epilepsy in human (Wang et al., 2015; Myers et al., 2018). Although the mechanisms underlying the epilepsy phenotypes remained unclear, so far, dysfunctions of VLGR1 related to the senso-neuronal defects in USH have been associated with fibrous linkers in membrane-membrane adhesions in retinal photoreceptor cells and auditory hair cells (McGee et al., 2006; Maerker et al., 2008) and with a putative role at the ribbon synapses of both types of sensory cells

[1]Institute of Molecular Physiology, Molecular Cell Biology, Johannes Gutenberg University, Hanns-Dieter-Hüsch-Weg 17, 55099 Mainz, Germany

[2]Medical Proteome Center, Institute for Ophthalmic Research, Eberhard Karls University of Tuebingen, 72074 Tuebingen, Germany

[3]Clinic of Visceral, Transplantation, Thoracic and Vascular Surgery & Clinic of Orthopedics, Traumatology and Plastic Surgery, Department of Surgery Research Laboratory, Leipzig University, 04301 Leipzig, Germany

[4]Lead contact

*Correspondence: wolfrum@uni-mainz.de

https://doi.org/10.1016/j.isci.2021.102283

(Reiners et al., 2005; Specht et al., 2009). At these sites, VLGR1 interacts with other USH proteins in the USH-related interactome (Mathur and Yang, 2015).

Recent and present systematic affinity proteomics analyses identified numerous new putative VLGR1 binding proteins (Knapp, et al., unpublished data, present study). Enrichment analysis and present comparisons with focal adhesion (FA) proteomes (Zaidel-Bar and Geiger, 2010; Schiller et al., 2011) and the adhesome database (http://www.adhesome.org) revealed numerous components of FAs in the VLGR1 interactome. FAs are large macromolecular assemblies arranged around transmembrane integrin dimers at the contact sites of the cell membrane with the extracellular matrix (ECM) (Geiger et al., 2009). Their dynamic assembly and disassembly play a central role in cell spreading and migration. FAs control these processes as hubs for bidirectional signaling: "inside-out" transmission of intracellular forces generated by contractions of the actin-myosin system to the ECM and *vice versa* "outside-in" signal transmission such as shear forces between the cell and the ECM from the environment to the cell interior (Shen et al., 2012; Sun et al., 2016).

The molecular composition and the dual function in adhesion and signal reception of ADGRs such as VLGR1 *per se* suggest a putative function at FAs. Here, we demonstrate that VLGR1 is an integral component of FAs essential for cell spreading and cell migration. We provide evidence that VLGR1 works as a metabotropic mechanoreceptor in FAs at the interface between the cell and its extracellular microenvironment. Our insights into the molecular and cellular function of VLGR1 in FAs enlighten the pathophysiology of the diseases related to VLGR1 dysfunction.

RESULTS

Affinity proteomics identifies FA-related proteins as putative VLGR1 interaction partners

To identify putative VLGR1-interacting proteins, we performed tandem affinity purifications (TAPs) from hTERT-RPE1 cells. We transfected these cells with Strep II Flag (SF)-tagged VLGR1 constructs (Figure 1A) and applied SF-TAP (Boldt et al., 2016). Eluted complexes were analyzed by liquid chromatography coupled with tandem mass spectrometry. Software Tool for Researching Annotations of Proteins-annotated proteomic data sets (Bhatia et al., 2009) revealed 478 proteins as putative VLGR1 interaction partners (Table S1). A comparison of these prey proteins with FA proteomes (Zaidel-Bar and Geiger, 2010; Schiller et al., 2011) and the adhesome database (http://www.adhesome.org) (Table S2) revealed 26 core FA molecules as putative interaction partners of VLGR1 (Figure 1, Table S3). Many classical FA core proteins such as integrin β1, integrin α3, and vinculin were enriched in the VLGR1 interactome of hTERT-RPE1 cells.

Integration of VLGR1 in FAs

To verify that VLGR1 is a component of FAs, we co-stained cell lines and primary cells for VLGR1, actin filaments (F-actin), and vinculin, a structural key component and molecular marker of FAs (Figure 2). Confocal microscopy of hTERT-RPE1 cells revealed VLGR1 localization in stripes at the end of F-actin bundles (Figure 2A), which were co-labeled for vinculin (Figure 2B). Quantification of VLGR1, vinculin, or F-actin staining in fluorescence intensity plots revealed substantial co-localization of these proteins (Figures 2C and 2D). We confirmed VLGR1 localization in FAs by double immunolabelling of VLGR1 and vinculin in mouse embryonic fibroblasts and primary astrocytes (Figure S1). Furthermore, we applied two additional FA markers: paxillin, present in the majority of adhesion sites including primordial focal complexes (FXs), and zyxin, absent from immature FXs but incorporated in more mature FAs (Zaidel-Bar et al., 2003). VLGR1 localized at both paxillin-associated adhesions (Figures S2A–S2C) and zyxin-labeled mature FAs (Figures S2B and S2D). The localization of VLGR1 in FAs was additionally confirmed by co-immunostaining of the FA markers vinculin or paxillin, respectively, and the two alternative VLGR1#2 and VLGR1#3 antibodies in both hTERT-RPE1 and primary astrocytes (Figure S3). Taken together, these findings indicate the presence of VLGR1 in all types of FAs, i.e., from nascent adhesions to *bona fide* FAs.

We further explored that the integration of VLGR1 in FAs using *in situ* proximity ligation assays (PLAs) (Figures 2E, S2E, and S2F). PLAs with pairs of two primary antibodies against VLGR1/vinculin, VLGR1/paxillin, and VLGR1/zyxin resulted in fluorescent PLA interaction spots indicating integration of VLGR1 into FA complexes (Figures 2E, S2E, and S2F). The PLA positive interaction spots were found near F-actin termini (Figures 2E, S2E, and S2F). In contrast, when antibodies were omitted, no PLA interaction spots were present (Figure S4). Overall, our results demonstrate that VLGR1 is part of the multi-protein complex in FAs.

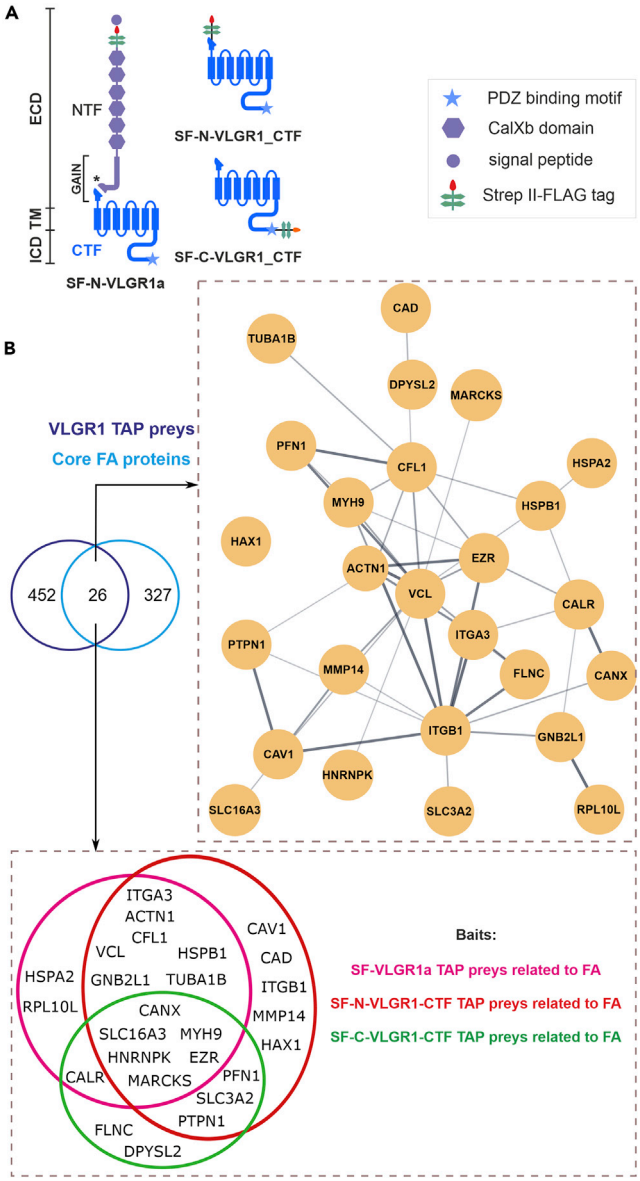

Figure 1. VLGR1 TAP associated putative FA proteins

(A) Full-length VLGR1a, N- or C- terminally VLGR1_CTF tagged with a Strep II- FLAG (SF)-tag used as baits in TAPs.

(B) Venn diagram showing an overlap of 26 proteins from VLGR1 TAP preys with previously published FA proteomes (Schiller et al., 2011; Zaidel-Bar and Geiger 2010) and the adhesome database (http://www.adhesome.org). STRING database analysis reveals the interconnection of overlapping proteins. Venn diagrams of FA preys found in the different VLGR1 TAP baits. NTF, N-terminal fragment; CTF, C-terminal fragment; ICD, intracellular domain; TM, transmembrane domain; ECD, extracellular domain; SP, signal peptide; Calxβ, Calx-β domains; PBM, PDZ-binding motif; GAIN, GPCR autoproteolysis-inducing domain; * indicates GPS, G protein-coupled receptor proteolytic site. See also Tables S1, S2, and S3.

VLGR1 deficiency or absence alters FA morphology

Next, we analyzed the effect of VLGR1 depletion on the structure and morphology of FAs in hTERT-RPE1 cells and astrocytes obtained from *Vlgr1*-deficient mutant mice. We used *Vlgr1*-del7TM mice lacking VLGR1 or the VLGR1 7TM and ICD (McMillan and White, 2004) and *Drum B* mice lacking large parts of the NTF and the entire CTF (Figure 3). For VLGR1 depletion, we transfected hTERT-RPE1 cells with non-targeting control or validated *VLGR1*-specific siRNAs (Figures 3A–3C; for *VLGR1* siRNA validation see: Figure S5). Vinculin immunostaining revealed a decrease in the number and length of FAs in *VLGR1*-depleted cells compared with control cells (Figures 3A–3C). To quantify FA lengths, we grouped FAs into four

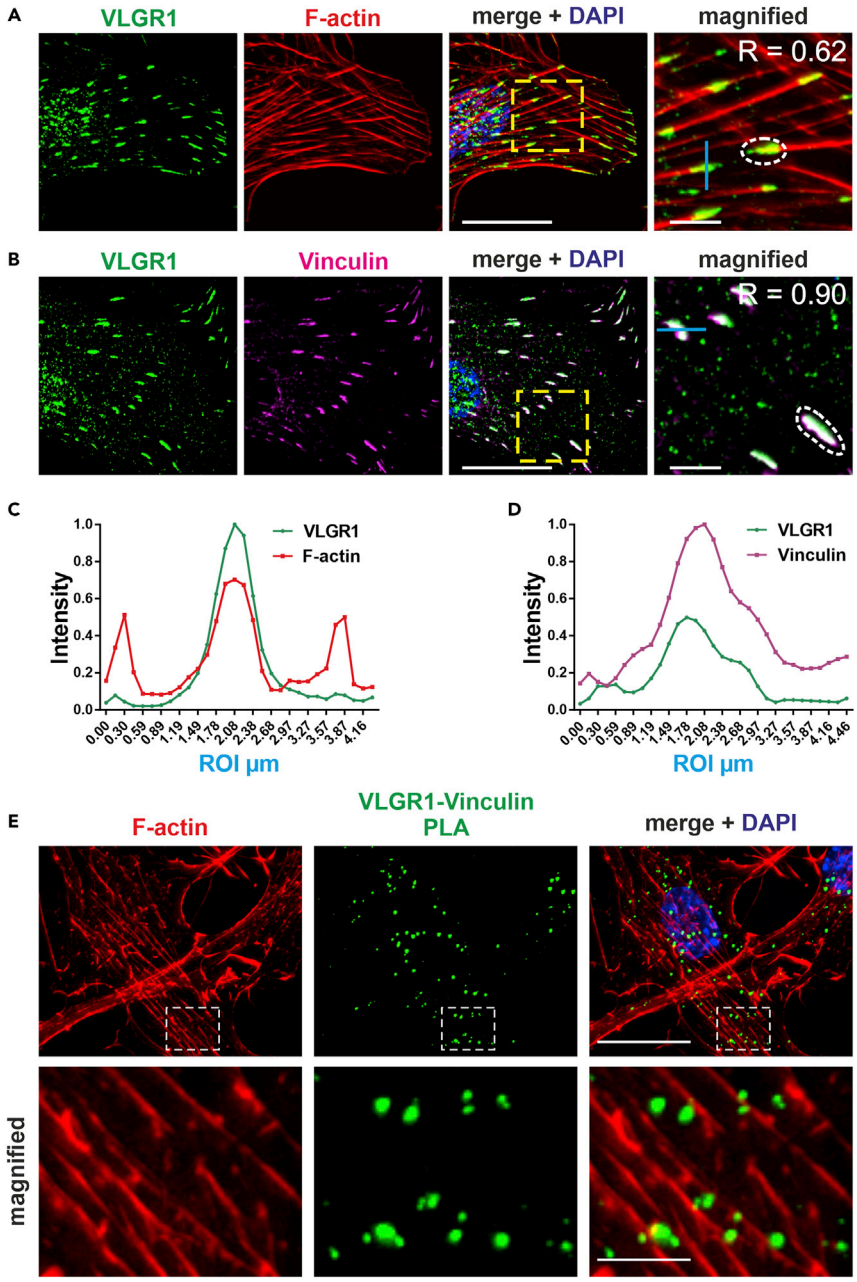

Figure 2. VLGR1 is localized at FAs

(A and B) Double labeling immunofluorescence of VLGR1 (green) and vinculin (magenta) in hTERT-RPE1 cells revealed a concentration of VLGR1 at the tip of F-actin stained by TRITC-phalloidin (red) (A) and in different forms of FAs (B). Pearson correlation coefficient R calculated in magnified images for white dotted region quantifies the degree of co-localization.

(C and D) Normalized fluorescence intensity plots of VLGR1 and F-actin (C) and VLGR1 and vinculin (D) share common peaks along the depicted blue line (ROI) in the magnified images indicating co-localization of both proteins.

(E) In a proximity ligation assay (PLA), the VLGR1-vinculin interaction dots (green) are in close proximity to F-actin. The boxed areas in the overlays are shown magnified. Nuclei are stained with DAPI (blue); scale bars: 25 µm, 5 µm magnified images. See also Figures S1–S4.

categories: nascent FXs 0-1 µm in length and more mature FAs of 1-2.5 µm, 2.5-5 µm, and 5-10 µm in length. VLGR1-depleted cells showed a higher percentage of shorter FAs 1-2.5 µm in length, while control cells contained more prominent and longer FAs (2.5-10 µm) (Figure 3C).

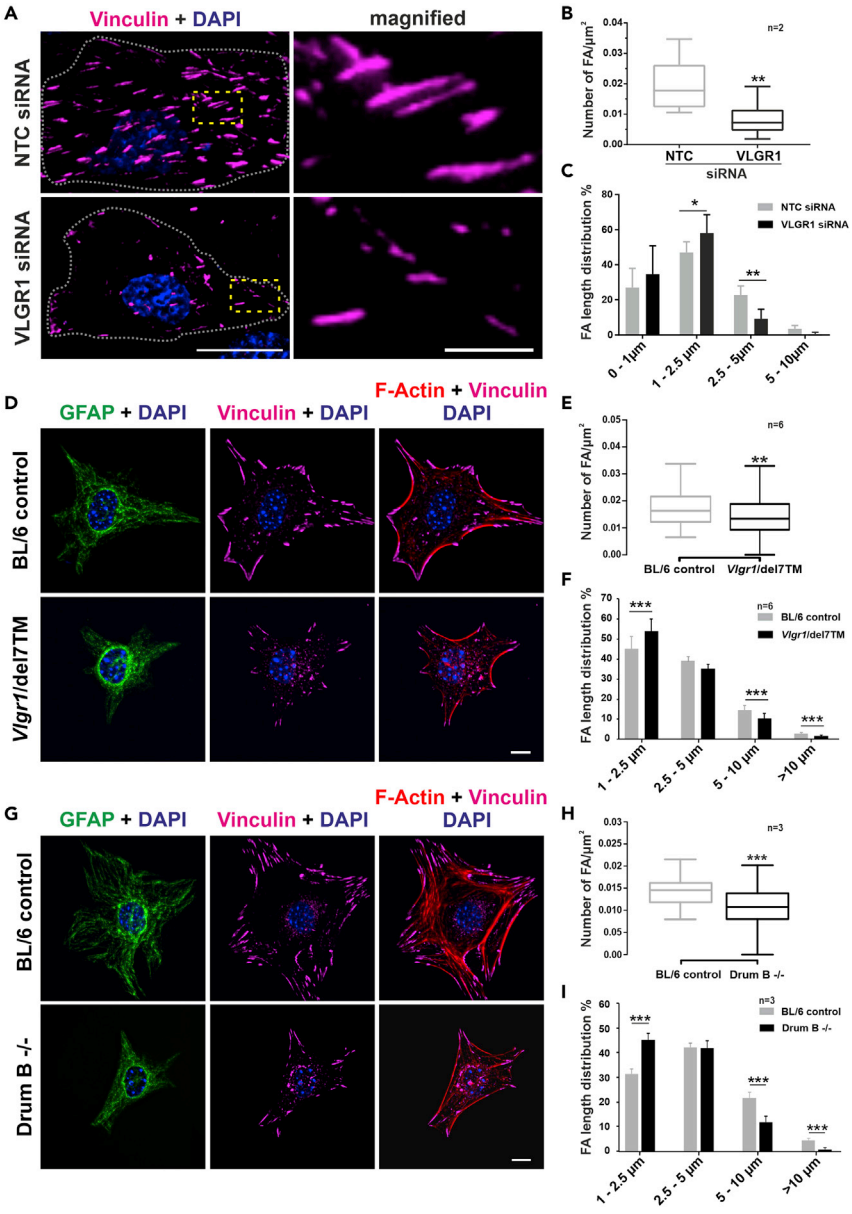

Figure 3. *VLGR1* deficiency alters FA morphology

Representative images of FAs in non-targeting control (NTC) and *VLGR1*-deficient hTERT-RPE1 cells (A–C) and in primary astrocytes from *Vlgr1*-del7TM (D–F) and *Drum B* mutant mice (G–I).

(A, D, G) FAs were stained for vinculin (magenta), F-actin with TRITC-phalloidin (red), and nuclei with DAPI (blue); GFAP (green) was used as an astrocyte marker. FA number and length were reduced after *VLGR1* depletion in hTERT-RPE1 cells (B, C) and in primary astrocytes of both *Vlgr1* mutant mouse lines (E, F, H, I). (B) Twenty-five cells per condition, (C) 900 FAs per condition. (E) Twenty cells per condition, (F) ~1300-1700 FAs per category for control and ~200-1000 FAs for mutant astrocytes. (H) Twenty cells per condition, (I) ~950-1250 FAs per condition for control and ~410-510 FAs for mutant astrocytes. Scale bars: (A) 25 µm and 5 µm in magnified images; (D), (G) 10 µm.

Data represented in (B), (E), and (H) are shown as box plot, and statistical analyses were done using two-tailed Mann-Whitney *U* test. Data in (C), (F), and (I) are represented as mean ± SD. Statistical analyses were done using Sidak's multiple comparison test; *p ≤ 0.05, **p ≤ 0.01, ***p ≤ 0.001. See also Figure S5.

In astrocytes obtained from *Vlgr1*-deficient, *Vlgr1*-del7TM, and *Drum B* mutant mice, we also observed fewer and shorter FAs compared to wild-type (WT) control astrocytes (Figures 3D–3G). The consistency of the effects on FAs in the knockdown experiments and the *Vgr1*-del7TM and *Drum B* mutant cells further

supports the specificity of the siRNAs applied. Collectively, these data demonstrate that VLGR1 is crucial for FA assembly.

VLGR1 knockdown and absence delays cell spreading

The size, shape, and spreading of cells mainly depend on FAs (Chen et al., 2003; Leiss et al., 2008). *VLGR1*-deficient and mutant cells were smaller in comparison to the control cells treated with non-targeting siRNA (Figures 3A and 3D). To address the role of VLGR1 in cell spreading more directly, control and *VLGR1*-deficient cells were allowed to spread and analyzed at different time points. Control cells formed spontaneous lamellipodia at the cell periphery, whereas the majority of the *VLGR1*-deficient cells failed to form these structures (Figure 4A). *VLGR1*-deficient cells showed abnormal morphology such as defects in blebbing, a process necessary for plasma membrane protrusion during cell spreading and migration (Norman et al., 2010).

Cell spreading goes through distinct defined subsequent phases (Gauthier et al., 2012; Greiner et al., 2013). After seeding onto an adhesive surface, cells form FAs to adhere to the ECM and proceed through phase 1 (P1, non-contractile spreading), then phase 2 (P2, contractile spreading), and finally phase 3 (P3, polarization). We defined these cell spreading phases for HEK293T cells (Figure S6). To determine the role of VLGR1 in phase progression during cell spreading, we knocked down *VLGR1* and monitored the cell shape 30 min and 2.5 hr after seeding on a poly-lysine-coated surface (Figures 4B and 4C). We found that 30 min after seeding, ~78% of the control cells had reached P2, whereas ~75% of *VLGR1*-deficient cells were still in P1 (Figures 4B–4B′). After 2.5 hr, ~80% of control cells were polarized (P3), whereas most *VLGR1*-deficient cells remained in P1 or P2 (Figures 4C–4C′).

The ECM protein fibronectin promotes cell spreading of mammalian cells (Leiss et al., 2008). On fibronectin-coated surfaces, the cell size of *VLGR1*-deficient HEK293T cells was also reduced at both time points when compared to control cells (Figures 5A, 5A′, 5B, and 5B′). In addition, primary astrocytes of both *Vlgr1*-del7TM and *Drum B* mouse mutants also had reduced surface areas compared to WT Bl6 control astrocytes (Figures 5C and 5C′). Taken together, our data demonstrate that the absence or depletion of VLGR1 causes defects in cell spreading.

VLGR1 depletion decreases total FAK expression but increases pFAK397 levels

The dynamics of FAs are regulated by the focal adhesion kinase (FAK) known as a multifunctional adapter and non-receptor tyrosine kinase involved in integrin-mediated signaling at FAs (Lawson and Schlaepfer, 2012). Phosphorylation of different amino acid residues on FAK modulates FA functions. For example, autophosphorylation of FAK at Tyr397 (pFAK-397) is a determinant step for FA disassembly (Hamadi et al., 2005; Webb et al., 2004). To determine a potential role of VLGR1-FAK interaction at FAs, we examined the expression of FAK and pFAK-397 in *VLGR1*-deficient hTERT-RPE1 cells in Western blot analyses. *VLGR1* depletion resulted in a decrease of total FAK and an increase of pFAK-397 in comparison to control cells (Figure 6). These changes suggest that FAK has roles in downstream signaling of VLGR1.

VLGR1 stimulates cell migration

Next, we investigated the role of VLGR1 in unidirectional, collective cell migration. We grew hTERT-RPE1 cells and mouse primary astrocytes cells to confluency and then "scratched" a space in the monolayer and followed the cells as they polarized and moved into the cleared area (Figure 7). In these migrating cells, VLGR1 was predominantly localized at the ends of F-actin bundles in small vinculin-positive puncta, likely FXs (Figure 7A). The localization of VLGR1-stained FAs of variable size at the leading edge of migrating cells suggests a putative role of VLGR1 in the regulation of polarized cell migration. To address such a role, we explored the effects of reducing cellular VLGR1 levels in the kinetics and extent of wound closure in two types of cells (Figure 7B). Firstly, we compared the closure rates of control hTERT-RPE1 cells with rates using hTERT-RPE1 in which we had knocked down VLGR1. We also compared the closure rates of mouse primary astrocytes from WT and Vlgr1-del7TM. Quantification revealed that wound closure was delayed at all time points in VLGR1-deficient cells compared to control cells (Figures 7B–7D). These motility assays indicate that the migration capacity is impaired in VLGR1-deficient cells and suggest a role of VLGR1 in collective cell migration regulation.

The kinetics of the closure of a wound in a monolayer is influenced both by the rate of the movement of cells into the denuded area as well as the rate of cell proliferation of new cells filling the space. Because VLGR1

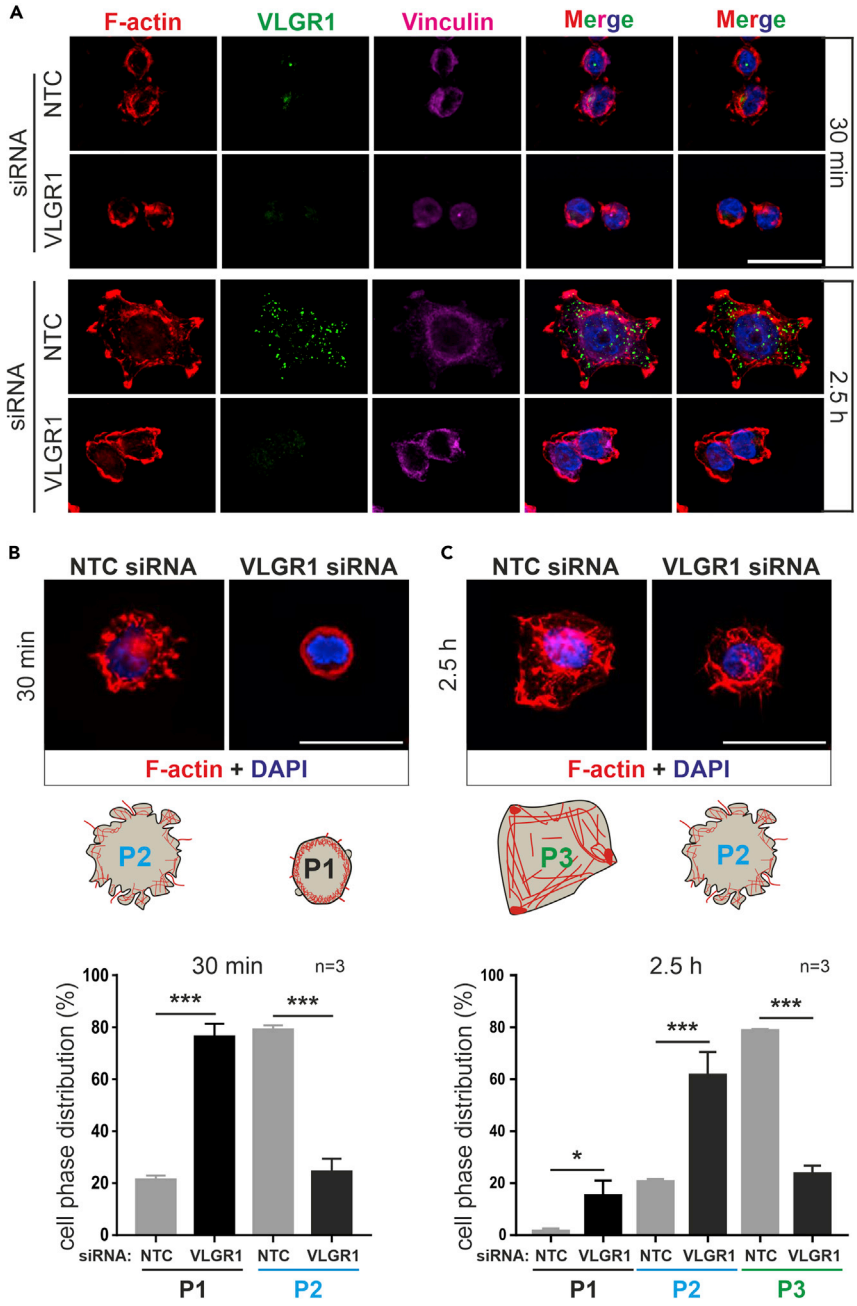

Figure 4. VLGR1-deficient cells show defects in phase progression during cell spreading

(A) Immunofluorescence staining of VLGR1 (green) of control (NTC) and VLGR1-depleted HEK293T cells subjected to cell spreading. VLGR1 is localized in the protruding cell membrane of control cells after 30 min and 2.5 hr of spreading. VLGR1 deficiency results in defective spreading. F-actin staining by TRITC-phalloidin (red) indicates cell areas. Vinculin (magenta) marks FAs.

(B and C) F-actin-stained control and VLGR1-depleted cells after 30 min (B) or 2.5 hr (C) of spreading on poly-L-coated coverslips. Cartoons represent stages of spreading for each condition. Blue: DAPI counterstain. (B′, C′) Quantification cells in different phases (P1, P2, and P3) of spreading. 300 cells per condition; scale bars, 25 μm. Data are represented as mean ± SD. Statistical evaluation was performed using Sidak's multiple comparison test; *$p \leq 0.05$, **$p \leq 0.01$, ***$p \leq 0.001$. See also Figure S6.

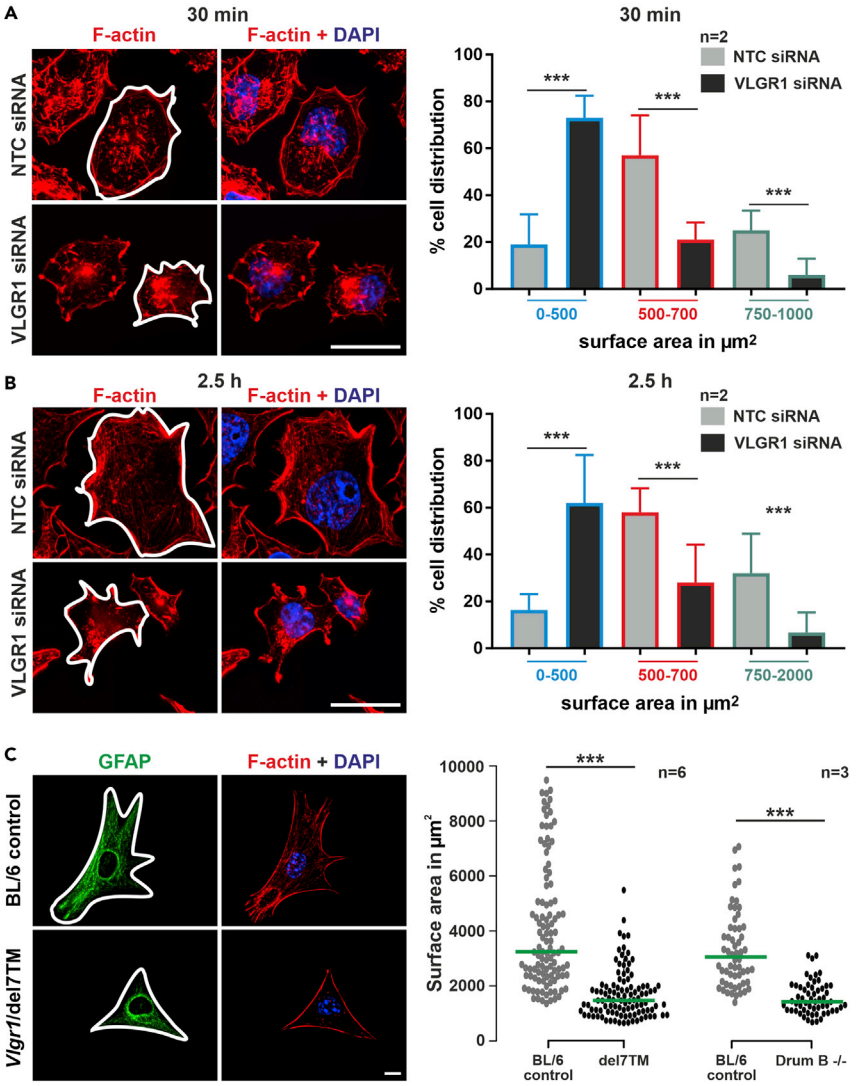

Figure 5. VLGR1 deficiency reduces cell surface area that is attached to the substrate

(A and B) HEK293T cells treated with non-targeting control (NTC) siRNA and VLGR1 siRNA were replated on fibronectin-coated coverslips and stained for F-actin (red, TRITC-phalloidin) and for nuclear DNA (blue, DAPI) at 30 min (A) and 2.5 hr (B).

(C) Primary astrocytes from *Vlgr1*-del7TM (C) stained for GFAP (green, astrocyte marker) and F-actin (red, TRITC-phalloidin); nuclei are stained with DAPI (blue). Quantifications of cell surface areas (white outline) by Fiji revealed a defect in cell spreading in VLGR1-deficient cells at both time points (A′, B′) and in primary astrocytes of *Vlgr1*-del7TM and *Drum B* mutant mice (C′). Green lines in dot plots indicate median (A′, B′) n = 400-600 cells per condition, 3 independent experiments. (C′) n = 20-40 cells per condition, 6 independent experiments for *Vlgr1*-del7TM and 3 independent experiments for *Drum B* mutant mice. Scale bars: (A), (B), 25 µm; (C), 10 µm. Data are represented as mean ± SD. Statistical evaluation was performed using Sidak's multiple comparison test in (A) and (B) and two-tailed Student's t test was applied in (C), *p ≤ 0.05, **p ≤ 0.01, ***p ≤ 0.001.

knockdown lead to a low but significant decrease of about 10% in cell proliferation (Figure S7), it is possible that the observed decrease in wound closure is a result of decreased cell proliferation and not a decreased migration. Therefore, we additionally tested the role of *VLGR1* in cell migration using live-cell imaging of single cells, which is not influenced by cell proliferation. We found that the velocity of primary astrocytes of *Vlgr1*-del7TM mice significantly decreased when compared to WT control astrocytes (Figures 7E and 7F, Videos S1 and S2). Our wound healing and single-cell imaging results suggest that cell migration in VLGR1-deficient cells is impaired and indicate an important role of the VLGR1 in controlling cell migration.

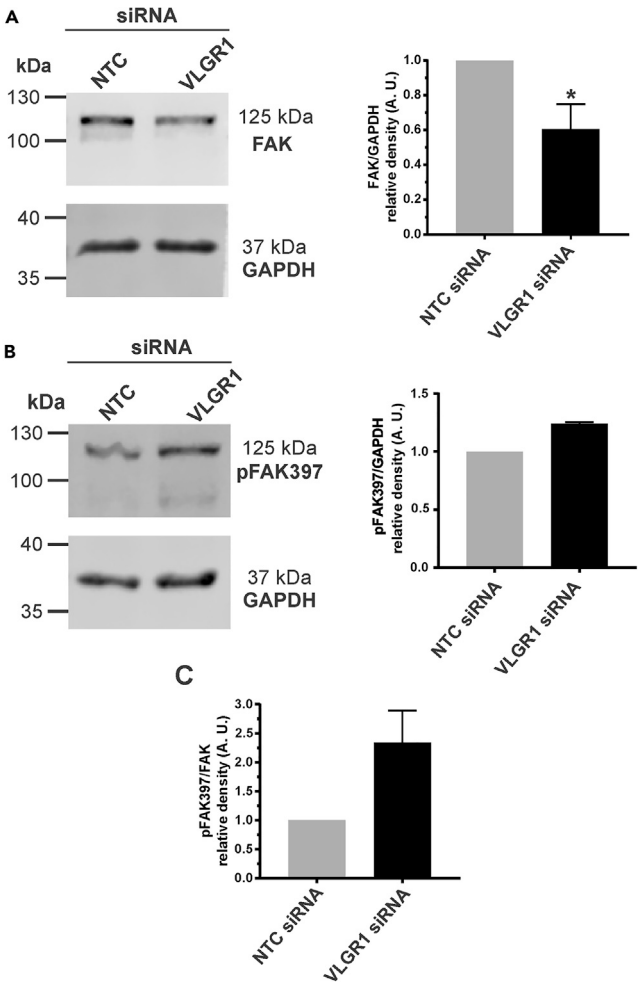

Figure 6. VLGR1 regulates FAK signaling

(A) Western blot analysis of FAK in control (NTC) and VLGR1-depleted hTERT-RPE1 cells and in the right panel, densitometric quantification of bands related to GAPDH expression in arbitrary units (A.U.).

(B) Western blot analysis of pFAK367 in control (NTC) and VLGR1-depleted hTERT-RPE1 cells and in the right panel densitometric quantification of band related to GAPDH expression in arbitrary units (A.U.).

(C) Relative expression pFAK397 and FAK. VLGR1 depletion leads to a significant decrease in total FAK and a slight increase of pFAK397. Data are represented as mean ± SD. Two-tailed Student's t test was applied, *$p < 0.05$, **$p < 0.01$, ***$p < 0.001$.

VLGR1 senses mechanical stimuli at FAs

There is growing evidence that ADGRs can act as mechanosensors that can transduce external mechanical forces into internal biochemical signals (Scholz et al., 2015). To investigate a role for VLGR1 in mechanosensing, we applied fluid shear stress to *VLGR1*-deficient and WT hTERT-RPE1 cells (Figure 8). We found that external mechanical force increased both the number and length of FAs in WT cells but not in untreated WT cells (Figures 8A–8C). Our results confirm previous studies under slightly different conditions with other cell types (Ponik and Pavalko, 2004; Lei et al., 2020). In WT cells, in addition to changes in FAs, we also observed that shear stress also decreased cell spreading on the substrate (Figure 8D). In contrast to WT cells, the number and length of FAs and cell spreading did not differ in shear stress-treated compared with untreated VLGR1-deficient hTERT-RPE1 cells (Figures 8A–8D). These findings indicate that VLGR1 participates in the transduction of mechanical force into a cellular response by remodeling FAs.

DISCUSSION

In the present study, we identified VLGR1 as an important component of FAs, highly dynamic macromolecular complexes coupled to the actin cytoskeleton (Zaidel-Bar and Geiger, 2010). FAs represent signaling

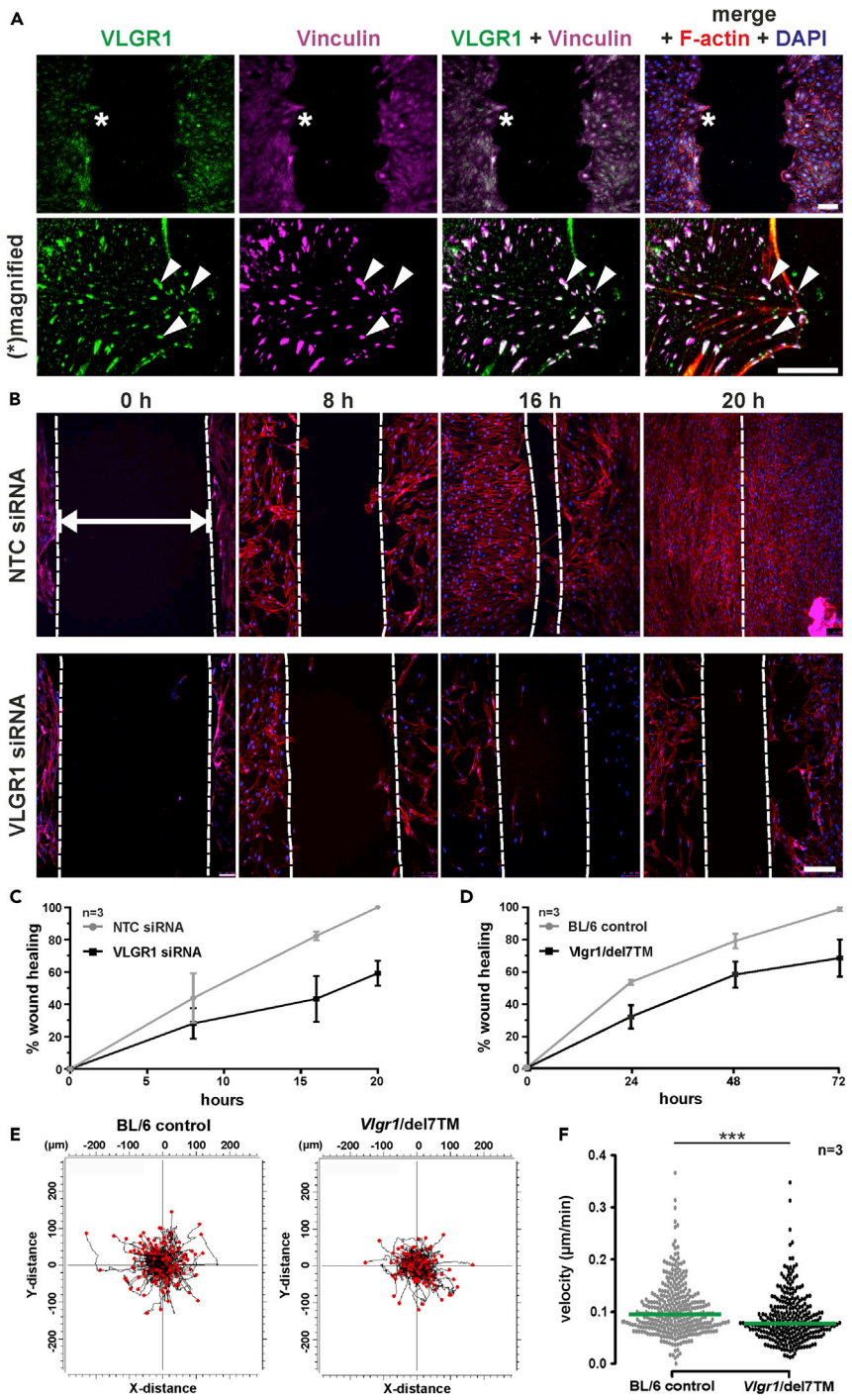

Figure 7. VLGR1 regulates cell migration

(A) VLGR1 (green) and vinculin (magenta) co-localize at the leading edge of hTERT-RPE1 cells migrating into the scratched wound area. *White asterisks* indicate the leading edge of migrating cells that are magnified in the lower panel showing focal complexes (*arrowheads*). F-actin (red); nuclear DNA (blue, DAPI).

(B) Wound closure analysis in control (NTC siRNA) and VLGR1-depleted (VLGR1 siRNA) cells at 0, 8, 16, and 20 hr. Dotted white lines indicate the wound area left open. *Double headed white arrow* indicates "wound" cleft. F-actin (red); DAPI stained nuclei (blue).

(C and D) (C) Wound closure rates in control and VLGR1-depleted hTERT-RPE1 cells and (D) in primary astrocytes of BL/6 wild-type control and *Vlgr1*-del7TM mice from 3 independent experiments each.

Figure 7. *Continued*

(E) Single-cell track plots of *Vlgr1*-del7TM and control mouse primary astrocytes; 24-hr video recorded with 15-min time interval. Each black line represents tracking paths of single cells. Red dots represent final points of migration. Images were taken at least 5 different spots; n = 329 cells for WT and n = 278 cells for *Vlgr1*-del7TM.

(F) Quantification of single cell migration revealing significant lower velocity of primary astrocytes in *Vlgr1*-del7TM mice. Green lines in dot plots indicate median. Scale bars: (A), top, 100 μm, middle, 25 μm, and bottom, 15 μm; (B), 200 μm. Data are represented as mean ± SD. Two-tailed Student's t test was applied in (C); *p ≤ 0.05, **p ≤ 0.01, ***p ≤ 0.001. See also Videos S1 and S2.

hubs that control cell adhesion and migration in response to internal or environmental cues (Geiger et al., 2009; Shen et al., 2012). Although the dual function of ADGRs in cell adhesion and sensing predestines ADGRs for signaling at cell adhesions, none of the 33 human ADGRs has been found in FAs to date.

VLGR1 associates with the FA core promoting FA maturation and dynamics

We provide several lines of evidence that VLGR1 is a component of FA. First, we identified many FA-related molecules as putative VLGR1 interacting proteins by TAP-based affinity proteomics performed in two different human cell lines (present study; Knapp et al., unpublished data), indicating that VLGR1 is a component of FAs. This is also confirmed by a quasi "reciprocal" proteomic approach, which revealed VLGR1 in the proteome of purified chemical cross-linked FAs of murine fibroblasts (Schiller et al., 2013). Secondly, VLGR1 co-localizes with molecular markers and core components of FAs present in several cell lines and primary cells. Thirdly, the physical interaction and thus close proximity of VLGR1 with other FA structural core components is strengthened by our *in situ* PLA data.

The presence of VLGR1 in immature nascent FXs at the leading edge of migrating cells suggests that its signaling may control the dynamics of FAs during their growth and maturation. Indeed, the formation of FAs is stunted in *VLGR1*-depleted cells: all analyzed cell types display smaller and less abundant FAs. A similar phenotype has been observed in cells deficient for FA core molecules known to participate in the regulation of FA dynamics and function (Raghavan et al., 2003; Saunders et al., 2006). Taken together, these findings identify VLGR1 as the first ADGR present at the protein cluster of FAs controlling FA dynamics.

VLGR1 in FA complexes establishes cell spreading and drives cell migration

FAs are signaling centers for the transformation and integration of signals between the ECM and interior of the cell, which are essential for the regulation of cell spreading and migration (Wozniak et al., 2004; Leiss et al., 2008). Here, we demonstrate that VLGR1 depletion reduces the kinetics of cell spreading and cell migration indicating that VLGR1 at FAs ensures the correct course of both processes. Defective cell spreading is a characteristic phenotype of cells deficient for FA signaling and signaling mediator molecules (Raghavan et al., 2003; Schiller et al., 2013; Thompson et al., 2014). Cell spreading is a crucial prerequisite for cell migration, and both processes require the coordination of the same subcellular molecular pathways (Kassianidou et al., 2019). Therefore, it is not surprising that VLGR1 deficiency also decreases cell migration. Consistently, cells deficient for the FA signaling molecules show decreased migration abilities (Fang et al., 2016; Colburn and Jones, 2017).

The dynamics and activity of FA components are vital for cell migration (Wozniak et al., 2004). One of the key players in the regulation of FA dynamics is FAK, and its ablation results in decreased cell migration (Sieg et al., 2000). Here, we show that VLGR1 depletion alters FAK protein expression and its physiological status, as seen by a decrease of total FAK and increase of FAK phosphorylated at tyrosine 397 (pFAK-397). VLGR1-mediated signaling may control proteostasis of the FAK protein at FAs. One potential target for this is the protease calpain, which mediates the cleavage and degradation of FAK at FAs (Chan et al., 2010). Interestingly, autophosphorylation of FAK at tyrosine 397 is a determinant step for FA disassembly (Webb et al., 2004; Hamadi et al., 2005) and correlates with the decrease in cell migration rates (Kim and Wirtz, 2013) which is line with our observations in *VLGR1*-depleted cells. Taken together, the absence of VLGR1 dysregulates FA signaling pathways and likely promotes the pathways underlying FA disassembly leading to reduced cell migration.

VLGR1 is a metabotropic mechanosensor in FAs

FAs act as supramolecular hubs for sensing and transmission of mechanical signals between the cell and its microenvironment (Gardel et al., 2010). In these adhesion complexes, integrins are key molecules of the

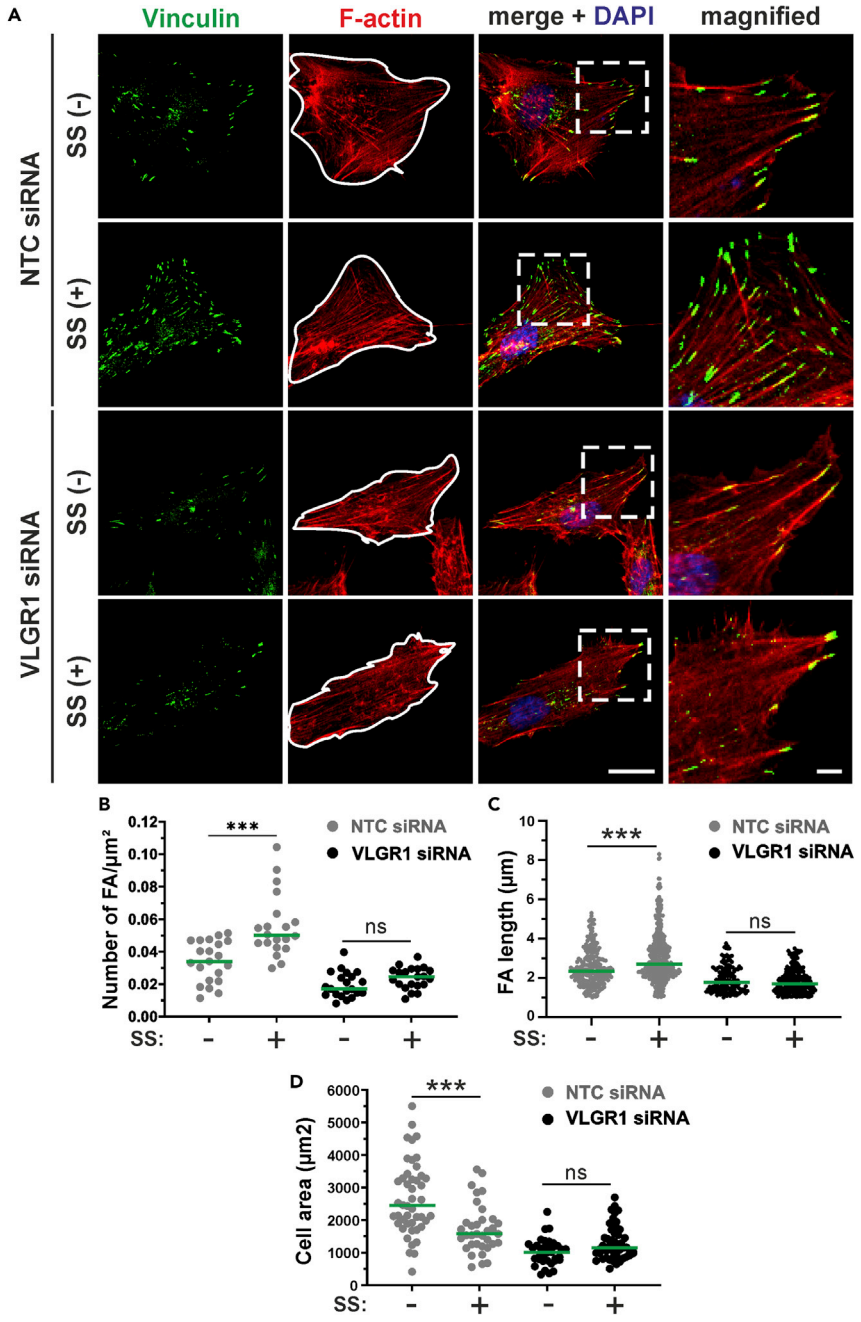

Figure 8. VLGR1 senses mechanical stimuli at FAs

(A) Analysis of FAs stained for vinculin (green) and cell area (*white lines*) in control (NTC siRNA) and VLGR1-depleted (VLGR1 siRNA) hTERT-RPE1 cells induced with (SS +) or without shear stress (SS -). Scale bars: 25 µm

(B–D) (B and C) Quantification of FA number (B), FA length (C), and of the cell area (D) in control and VLGR1-depleted cells under shear stress (SS +) and static conditions (SS -). Six hundred to 2000 FAs per condition; 50 cell areas per condition. Green lines in dot plots indicate median values. Data are represented as mean ± SD. Statistical evaluation was performed by Sidak's multiple comparison tests; *p ≤ 0.05, **p ≤ 0.01, ***p ≤ 0.001.

bidirectional mechanical signaling (Sun et al., 2016). These transmembrane dimers transmit inside-out sensing of the intracellular tension generated by the actin-myosin system to the ECM but also sense physical properties of the ECM in an outside-in manner. Tensile forces between integrins and ECM molecules are transduced via cytoskeletal adapter proteins such as the molecular clutch protein talin (Elosegui-Artola

et al., 2016). However, little is known about the participation of ADGRs in FA mechanosensation. Here, we show that VLGR1 is also essential for cells to respond to the mechanical stimuli at FAs in a shear stress paradigm. This indicates VLGR1 acts as a metabotropic mechanosensor in outside-in sensing at FAs, controlling FA assembly and function.

Our findings are consistent with emerging evidence for other ADGRs acting as mechanosensors, sensing mechanical signals from the extracellular environment (Scholz et al., 2015; Langenhan, 2020). In the peripheral nervous system, GPR126/ADGRG6 senses the mechanical property of the ECM in the basal lamina during Schwan cell development (Mogha et al., 2016). Other ADGRs also detect mechanical changes in a higher dynamic range such as shear, vibration, or stretch (Langenhan et al., 2016). In *Drosophila*, Cirl, an ADGR homolog of vertebrate latrophilins/ADGRLs, is essential for the perception of sound, stretch, or touch in mechanosensitive sensory cells (Scholz et al., 2015). VLGR1 may respond to mechanical forces in a wide dynamic range at FAs, including static mechanical forces which are present during cell spreading and assembly of FAs and more dynamic forces emerging during cell migration and shear stress, respectively.

Liebscher et al. (2014) discovered peptide sequences C-terminal to the GPS motif in the GAIN domain of ADGRs that act as a tethered endogenous agonist which is in line with their general function as mechanosensors (Langenhan et al., 2016). Mechanical forces, transmitted by the ECD, may dislodge this so-called "*Stachel*" into the extracellular grooves/surface of the 7TM domain of the receptor. Recently, we identified an 11-amino acid peptide as the *Stachel* sequence in the GAIN domain of VLGR1 (Knapp et al., unpublished data) indicating that the mechanical stimulation of VLGR1 may also occur through the conserved tethered agonism. Taken together, our findings suggest that mechanical stimuli at FAs are received and transduced by VLGR1.

VLGR1 activation likely couples to a $G\alpha_i$-mediated signaling downstream pathway (Hu et al., 2014; Knapp et al., unpublished data). Although details still remain elusive, our data indicate a cross talk between VLGR1 and FAK signaling. In any case, VLGR1 deficiency dysregulates FAK expression and activation.

How do our findings relate to diseases caused by defects in VLGR1?

At first glance, our data shown here do not provide novel insights into pathomechanisms underlying to epilepsy and USH. However, VLGR1 is highly expressed in the developing CNS (McMillan and White, 2010), in which cell migration is an important feature. Interestingly, defects in migration pathways have recently been linked to increased susceptibility to epilepsy (Qin et al., 2017; Liu et al., 2020). Accordingly, cell migration defects described here may be the cellular basis for the susceptibility to audiogenic seizures and epilepsy associated with VLGR1 dysfunction.

USH2C is characterized by hearing and vision deficiencies. In both affected sensory cells, VLGR1 is an essential component of extracellular fibers, namely the ankle links present between the neighboring stereocilia of developing hair cells (McGee et al., 2006) and fibrous links associated with sensory cilia of photoreceptors (Maerker et al., 2008). There is evidence that the ankle links sense the proximity between neighboring stereocilia, which is needed to refine and shape the typical V-form hair bundle at the hair cell surface (Richardson and Petit, 2019). Within these links, VLGR1 may serve as the mechanosensor detecing mechanical forces between neighboring stereocilia. The mechanical forces acting on the VLGR1-based fibrous links at the ciliary base of photoreceptors are even less clear. They may contribute to the alignment of the photoreceptor cilium and the outer segment toward the incoming light (Enoch, 1978; Wolfrum, 1995). However, based on the present findings, further research will be required to elucidate the pathomechanisms caused by defects in VLGR1.

Conclusion

We identified and validated VLGR1 as the first ADGR in the macromolecular cluster of proteins comprising FAs. We show that VLGR1 is vital component of FAs and provide novel insight into the molecular composition and function of FAs. VLGR1 is crucial for key functions of FAs in processes such as cell spreading and cell migration. We provide evidence that VLGR1 functions as metabotropic mechanosensor at FAs sensing mechanical cues from the extracellular environment of the cell during these processes. These findings also provide fresh basis for explaining the pathomechanisms underlying VLGR1-associated diseases.

Limitations of the study

Our study provides several lines of molecular and cellular evidence for the role of VLGR1 in FAs as a metabotropic mechanosensor that regulates cell spreading and migration. Further studies are needed to gain molecular and mechanistic insights into mechanostimulation of VLGR1 receptors in FAs, for example, using non-cleavable VLGR1 mutants to clarify whether this involves release of the NTF from its CTF base. Our data also show that a signaling pathway downstream of VLGR1 interacts with the FAK pathway. However, deciphering the details of the cross talk of FAK and integrin signaling in FAs is reserved for future studies. We propose that defective cell migration and mechanosensation that we observed in VLGR1 deficiency could trigger the development of epilepsy and USH, but further research is needed to elucidate the pathomechanisms caused by VLGR1 defects leading to these diseases.

Resource availability

Lead contact

Further information and requests for resources and data should be directed to the lead contact, Uwe Wolfrum, Institute of Molecular Physiology, Molecular Biology, Johannes Gutenberg University of Mainz, Hanns-Dieter-Hüsch-Weg 17 , D-55099 Mainz, Germany (wolfrum@uni-mainz.de).

Materials availability

This study did not generate new unique reagents.

Data and code availability

Original/source data for all figures presented in the paper are available from the lead contact upon request.

METHODS

All methods can be found in the accompanying transparent methods supplemental file.

SUPPLEMENTAL INFORMATION

Supplemental information can be found online at https://doi.org/10.1016/j.isci.2021.102283.

ACKNOWLEDGMENTS

This work was supported by the German Research Council (DFG) for 2149 "Elucidation of Adhesion-GPR signaling" WO 548/8 (U.W.) and AU132/8 (GA), European Community "SYSCILIA" [FP7/2009/241955] (M.U., U.W.), and Foundation Fighting Blindness (FFB) PPA-0717-0719-RAD (M.U., U.W.). In addition, we thank Drs. Karl Fath, Kerstin Nagel-Wolfrum, Helen May-Simera, Sarita Rani Patnaik, and Aziz El-Amraoui for helpful discussions and language editing.

AUTHOR CONTRIBUTIONS

B.K. conducted the initial TAP analysis; K.B., N.H., and M.U. carried out mass spectrometry analysis; B.K. and D.K.K. analyzed TAP datasets. B.E.G. performed the experiments with primary astrocytes including life cell imaging and D.K.K. conducted most other experiments. G.A. along with D.K.K. contributed to shear stress experiments. U.W. and D.K.K. designed the studies and wrote the manuscript. All authors read and approved the final manuscript.

DECLARATION OF INTERESTS

The authors declare that there is no conflict of interest.

Received: December 1, 2020
Revised: February 12, 2021
Accepted: March 3, 2021
Published: April 23, 2021

REFERENCES

Bhatia, V.N., Perlman, D.H., Costello, C.E., and Mccomb, M.E. (2009). Software tool for researching annotations of proteins: open-source protein annotation software with data visualization. Anal Chem. *81*, 9819–9823.

Boldt, K., Van Reeuwijk, J., Lu, Q., Koutroumpas, K., Nguyen, T.M., Texier, Y., Van Beersum, S.E., Horn, N., Willer, J.R., Mans, D.A., et al.; UK10K Rare Diseases Group (2016). An organelle-specific protein landscape identifies novel diseases and molecular mechanisms. Nat. Commun. *7*, 11491.

Chan, K.T., Bennin, D.A., and Huttenlocher, A. (2010). Regulation of adhesion dynamics by calpain-mediated proteolysis of focal adhesion kinase (FAK). J. Biol. Chem. *285*, 11418–11426.

Chen, C.S., Alonso, J.L., Ostuni, E., Whitesides, G.M., and Ingber, D.E. (2003). Cell shape provides global control of focal adhesion assembly. Biochem. Biophys. Res. Commun. *307*, 355–361.

Colburn, Z.T., and Jones, J.C. (2017). alpha6beta4 integrin regulates the collective migration of epithelial cells. Am. J. Respir. Cell Mol. Biol. *56*, 443–452.

Elosegui-Artola, A., Oria, R., Chen, Y., Kosmalska, A., Perez-Gonzalez, C., Castro, N., Zhu, C., Trepat, X., and Roca-Cusachs, P. (2016). Mechanical regulation of a molecular clutch defines force transmission and transduction in response to matrix rigidity. Nat. Cell Biol. *18*, 540–548.

Enoch, J.M. (1978). The relationship between retinal receptor orientation and photoreceptor optics. Int. Ophthalmol. Clin. *18*, 41–80.

Fang, K.P., Dai, W., Ren, Y.H., Xu, Y.C., Zhang, S.M., and Qian, Y.B. (2016). Both Talin-1 and Talin-2 correlate with malignancy potential of the human hepatocellular carcinoma MHCC-97 L cell. BMC Cancer *16*, 45.

Gardel, M.L., Schneider, I.C., Aratyn-Schaus, Y., and Waterman, C.M. (2010). Mechanical integration of actin and adhesion dynamics in cell migration. Annu. Rev. Cell Dev. Biol. *26*, 315–333.

Gauthier, N.C., Masters, T.A., and Sheetz, M.P. (2012). Mechanical feedback between membrane tension and dynamics. Trends Cell Biol. *22*, 527–535.

Geiger, B., Spatz, J.P., and Bershadsky, A.D. (2009). Environmental sensing through focal adhesions. Nat. Rev. Mol. Cell Biol. *10*, 21–33.

Greiner, A.M., Chen, H., Spatz, J.P., and Kemkemer, R. (2013). Cyclic tensile strain controls cell shape and directs actin stress fiber formation and focal adhesion alignment in spreading cells. PLoS One *8*, e77328.

Hamadi, A., Bouali, M., Dontenwill, M., Stoeckel, H., Takeda, K., and Ronde, P. (2005). Regulation of focal adhesion dynamics and disassembly by phosphorylation of FAK at tyrosine 397. J. Cell Sci. *118*, 4415–4425.

Hu, Q.X., Dong, J.H., Du, H.B., Zhang, D.L., Ren, H.Z., Ma, M.L., Cai, Y., Zhao, T.C., Yin, X.L., Yu, X., et al. (2014). Constitutive Galphai coupling activity of very large G protein-coupled receptor 1 (VLGR1) and its regulation by PDZD7 protein. J. Biol. Chem. *289*, 24215–24225.

Kassianidou, E., Probst, D., Jager, J., Lee, S., Roguet, A.L., Schwarz, U.S., and Kumar, S. (2019). Extracellular matrix geometry and initial adhesive position determine stress fiber network organization during cell spreading. Cell Rep. *27*, 1897–1909.e4.

Kim, D.H., and Wirtz, D. (2013). Focal adhesion size uniquely predicts cell migration. FASEB J. *27*, 1351–1361.

Knapp, B., Roedig, J., Boldt, K., Krzysko, J., Horn, N., Ueffing, M., and Wolfrum, U. (2019). Affinity proteomics identifies novel functional modules related to adhesion GPCRs. Ann. N Y Acad. Sci. *1456*, 144–167.

Knierim, A.B., Rothe, J., Cakir, M.V., Lede, V., Wilde, C., Liebscher, I., Thor, D., and Schoneberg, T. (2019). Genetic basis of functional variability in adhesion G protein-coupled receptors. Sci. Rep. *9*, 11036.

Langenhan, T. (2020). Adhesion G protein-coupled receptors-Candidate metabotropic mechanosensors and novel drug targets. Basic Clin. Pharmacol. Toxicol. *126* (*Suppl 6*), 5–16.

Langenhan, T., Piao, X., and Monk, K.R. (2016). Adhesion G protein-coupled receptors in nervous system development and disease. Nat. Rev. Neurosci. *17*, 550–561.

Lawson, C., and Schlaepfer, D.D. (2012). Integrin adhesions: who's on first? What's on second? Connections between FAK and talin. Cell Adhes. Migr. *6*, 302–306.

Lei, X., Wu, H., Song, Y., Liu, B., Zhang, S.S., Li, J.Q., Bi, L., and Pei, G.X. (2020). Effects of cyclic fluid stress at different frequencies on behaviors of cells incubated on titanium alloy. Biochem. Biophys. Res. Commun. *522*, 100–106.

Leiss, M., Beckmann, K., Giros, A., Costell, M., and Fassler, R. (2008). The role of integrin binding sites in fibronectin matrix assembly in vivo. Curr. Opin. Cell Biol. *20*, 502–507.

Liebscher, I., Schon, J., Petersen, S.C., Fischer, L., Auerbach, N., Demberg, L.M., Mogha, A., Coster, M., Simon, K.U., Rothemund, S., et al. (2014). A tethered agonist within the ectodomain activates the adhesion G protein-coupled receptors GPR126 and GPR133. Cell Rep. *9*, 2018–2026.

Liu, J.Y.W., Dzurova, N., Al-Kaaby, B., Mills, K., Sisodiya, S.M., and Thom, M. (2020). Granule cell dispersion in human temporal lobe epilepsy: proteomics investigation of neurodevelopmental migratory pathways. Front. Cell Neurosci. *14*, 53.

Maerker, T., Van Wijk, E., Overlack, N., Kersten, F.F., Mcgee, J., Goldmann, T., Sehn, E., Roepman, R., Walsh, E.J., Kremer, H., and Wolfrum, U. (2008). A novel Usher protein network at the periciliary reloading point between molecular transport machineries in vertebrate photoreceptor cells. Hum. Mol. Genet. *17*, 71–86.

Mathur, P., and Yang, J. (2015). Usher syndrome: hearing loss, retinal degeneration and associated abnormalities. Biochim. Biophys. Acta *1852*, 406–420.

McGee, J., Goodyear, R.J., Mcmillan, D.R., Stauffer, E.A., Holt, J.R., Locke, K.G., Birch, D.G., Legan, P.K., White, P.C., Walsh, E.J., and Richardson, G.P. (2006). The very large G-protein-coupled receptor VLGR1: a component of the ankle link complex required for the normal development of auditory hair bundles. J. Neurosci. *26*, 6543–6553.

McMillan, D.R., and White, P.C. (2004). Loss of the transmembrane and cytoplasmic domains of the very large G-protein-coupled receptor-1 (VLGR1 or Mass1) causes audiogenic seizures in mice. Mol. Cell Neurosci. *26*, 322–329.

McMillan, D.R., and White, P.C. (2010). Studies on the very large G protein-coupled receptor: from initial discovery to determining its role in sensorineural deafness in higher animals. Adv. Exp. Med. Biol. *706*, 76–86.

Mogha, A., Harty, B.L., Carlin, D., Joseph, J., Sanchez, N.E., Suter, U., Piao, X., Cavalli, V., and Monk, K.R. (2016). Gpr126/Adgrg6 has Schwann cell autonomous and nonautonomous functions in peripheral nerve injury and repair. J. Neurosci. *36*, 12351–12367.

Myers, K.A., Nasioulas, S., Boys, A., Mcmahon, J.M., Slater, H., Lockhart, P., Sart, D.D., and Scheffer, I.E. (2018). ADGRV1 is implicated in myoclonic epilepsy. Epilepsia *59*, 381–388.

Norman, L.L., Brugues, J., Sengupta, K., Sens, P., and Aranda-Espinoza, H. (2010). Cell blebbing and membrane area homeostasis in spreading and retracting cells. Biophys. J. *99*, 1726–1733.

Ponik, S.M., and Pavalko, F.M. (2004). Formation of focal adhesions on fibronectin promotes fluid shear stress induction of COX-2 and PGE2 release in MC3T3-E1 osteoblasts. J. Appl. Physiol. (1985) *97*, 135–142.

Qin, R., Cao, S., Lyu, T., Qi, C., Zhang, W., and Wang, Y. (2017). CDYL deficiency disrupts neuronal migration and increases susceptibility to epilepsy. Cell Rep. *18*, 380–390.

Raghavan, S., Vaezi, A., and Fuchs, E. (2003). A role for alphabeta1 integrins in focal adhesion function and polarized cytoskeletal dynamics. Dev. Cell *5*, 415–427.

Reiners, J., Van Wijk, E., Marker, T., Zimmermann, U., Jurgens, K., Te Brinke, H., Overlack, N., Roepman, R., Knipper, M., Kremer, H., and Wolfrum, U. (2005). Scaffold protein harmonin (USH1C) provides molecular links between Usher syndrome type 1 and type 2. Hum. Mol. Genet. *14*, 3933–3943.

Richardson, G.P., and Petit, C. (2019). Hair-bundle links: genetics as the gateway to function. Cold Spring Harb. Perspect. Med. *9*, a033142.

Saunders, R.M., Holt, M.R., Jennings, L., Sutton, D.H., Barsukov, I.L., Bobkov, A., Liddington, R.C., Adamson, E.A., Dunn, G.A., and Critchley, D.R. (2006). Role of vinculin in regulating focal adhesion turnover. Eur. J. Cell Biol. *85*, 487–500.

Schiller, H.B., Friedel, C.C., Boulegue, C., and Fassler, R. (2011). Quantitative proteomics of the integrin adhesome show a myosin II-dependent recruitment of LIM domain proteins. EMBO Rep. *12*, 259–266.

Schiller, H.B., Hermann, M.R., Polleux, J., Vignaud, T., Zanivan, S., Friedel, C.C., Sun, Z., Raducanu, A., Gottschalk, K.E., Thery, M., et al. (2013). beta1- and alphav-class integrins cooperate to regulate myosin II during rigidity sensing of fibronectin-based microenvironments. Nat. Cell Biol. *15*, 625–636.

Scholz, N., Gehring, J., Guan, C., Ljaschenko, D., Fischer, R., Lakshmanan, V., Kittel, R.J., and Langenhan, T. (2015). The adhesion GPCR latrophilin/CIRL shapes mechanosensation. Cell Rep. *11*, 866–874.

Shen, B., Delaney, M.K., and Du, X. (2012). Inside-out, outside-in, and inside-outside-in: G protein signaling in integrin-mediated cell adhesion, spreading, and retraction. Curr. Opin. Cell Biol. *24*, 600–606.

Sieg, D.J., Hauck, C.R., Ilic, D., Klingbeil, C.K., Schaefer, E., Damsky, C.H., and Schlaepfer, D.D. (2000). FAK integrates growth-factor and integrin signals to promote cell migration. Nat. Cell Biol. *2*, 249–256.

Specht, D., Wu, S.B., Turner, P., Dearden, P., Koentgen, F., Wolfrum, U., Maw, M., Brandstatter, J.H., and Tom Dieck, S. (2009). Effects of presynaptic mutations on a postsynaptic Cacna1s calcium channel colocalized with mGluR6 at mouse photoreceptor ribbon synapses. Invest Ophthalmol. Vis. Sci. *50*, 505–515.

Sun, Z., Guo, S.S., and Fassler, R. (2016). Integrin-mediated mechanotransduction. J. Cell Biol. *215*, 445–456.

Thompson, P.M., Tolbert, C.E., Shen, K., Kota, P., Palmer, S.M., Plevock, K.M., Orlova, A., Galkin, V.E., Burridge, K., Egelman, E.H., et al. (2014). Identification of an actin binding surface on vinculin that mediates mechanical cell and focal adhesion properties. Structure *22*, 697–706.

Wang, Y., Fan, X., Zhang, W., Zhang, C., Wang, J., Jiang, T., and Wang, L. (2015). Deficiency of very large G-protein-coupled receptor-1 is a risk factor of tumor-related epilepsy: a whole transcriptome sequencing analysis. J. Neurooncol. *121*, 609–616.

Webb, D.J., Donais, K., Whitmore, L.A., Thomas, S.M., Turner, C.E., Parsons, J.T., and Horwitz, A.F. (2004). FAK-Src signalling through paxillin, ERK and MLCK regulates adhesion disassembly. Nat. Cell Biol. *6*, 154–161.

Weston, M.D., Luijendijk, M.W., Humphrey, K.D., Moller, C., and Kimberling, W.J. (2004). Mutations in the VLGR1 gene implicate G-protein signaling in the pathogenesis of Usher syndrome type II. Am. J. Hum. Genet. *74*, 357–366.

Wolfrum, U. (1995). Centrin in the photoreceptor cells of mammalian retinae. Cell Motil. Cytoskeleton *32*, 55–64.

Wozniak, M.A., Modzelewska, K., Kwong, L., and Keely, P.J. (2004). Focal adhesion regulation of cell behavior. Biochim. Biophys. Acta *1692*, 103–119.

Zaidel-Bar, R., Ballestrem, C., Kam, Z., and Geiger, B. (2003). Early molecular events in the assembly of matrix adhesions at the leading edge of migrating cells. J. Cell Sci. *116*, 4605–4613.

Zaidel-Bar, R., and Geiger, B. (2010). The switchable integrin adhesome. J. Cell Sci *123*, 1385–1388.

iScience, Volume *24*

Supplemental information

Adhesion G protein-coupled receptor VLGR1/ADGRV1 regulates cell spreading and migration by mechanosensing at focal adhesions

Deva K. Kusuluri, Baran E. Güler, Barbara Knapp, Nicola Horn, Karsten Boldt, Marius Ueffing, Gabriela Aust, and Uwe Wolfrum

Supplemental Information

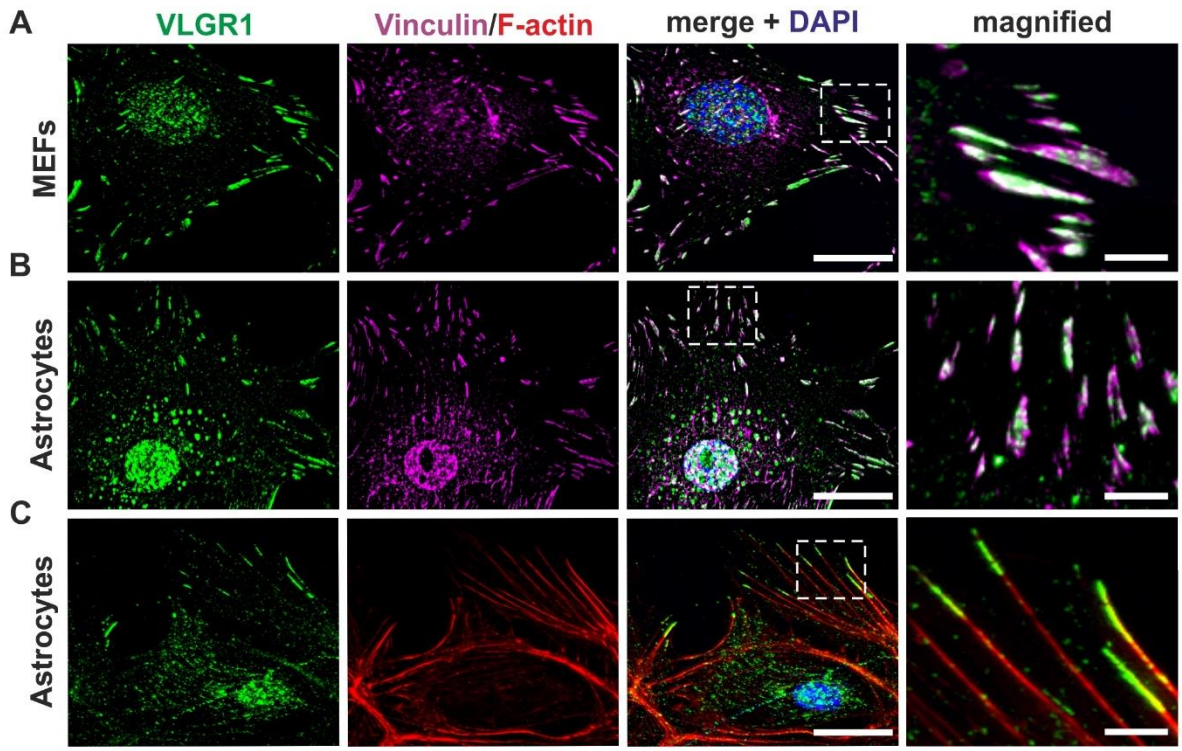

Figure S1. VLGR1 localization at FAs in different cell types, Related to Figure 2. (A) Subcellular localization of VLGR1 in FAs of cultured mouse embryonic fibroblasts (MEFs, A) and astrocytes (B). Immunofluorescence staining of VLGR1 (green), which is co-expressed with vinculin (magenta) in FAs. (C) VLGR1 localizes to the tip of F-actin in mouse astrocytes. Immunofluorescence staining of VLGR1 (green) and F-actin stained with TRITC-phalloidin (red). Scale bar, 25 μm; magnified panel, 5 μm. Nuclei were stained with DAPI (blue).

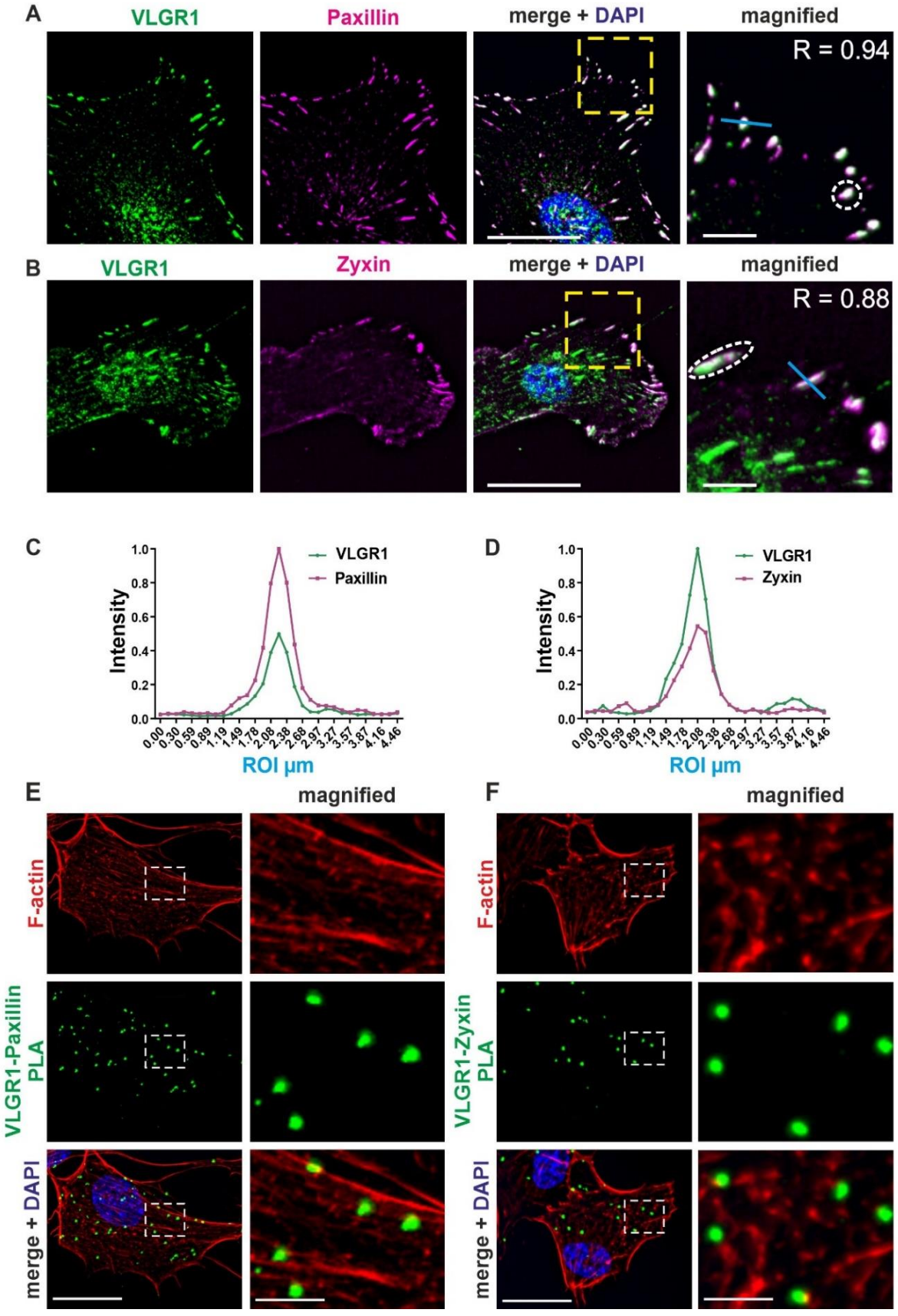
A
VLGR1
Paxillin
merge + DAPI
magnified
R = 0.94
B
VLGR1
Zyxin
merge + DAPI
magnified
R = 0.88
C
Intensity
VLGR1
Paxillin
ROI µm
D
Intensity
VLGR1
Zyxin
ROI µm
E
magnified
F-actin
VLGR1-Paxillin PLA
merge + DAPI
F
magnified
F-actin
VLGR1-Zyxin PLA
merge + DAPI

Figure S2. VLGR1 is localized at different forms of FAs, Related to Figure 2. (A-B) Immunofluorescence double labeling in hTERT-RPE1 cells revealed localization of VLGR1 (green) in nascent adhesions marked by paxillin (magenta, A), as well as mature adhesions stained with zyxin (magenta, B). The boxed areas in the overlays are shown at higher magnifications in the right column (magnified). Pearson coefficient (R) in magnified images for dotted region of interest (ROI; white) shows the degree of co-localization (positive values), indicated at the top of magnified image. Nuclei are stained with DAPI (blue). Scale bars: 25 µm, in magnified panel 5 µm. (C-D) Normalized fluorescence intensity plots of corresponding line scan (blue line) show co-localization of VLGR1 with paxillin (C), zyxin (D). (E-F) *In situ* proximity ligation assay (PLA) events (green dots) showing a close proximity localization of VLGR1 and nascent FA marker paxillin (E), VLGR1 and mature FA marker zyxin (F). TRITC-phalloidin (red) staining of F-actin was used to visualize cell area, nuclei were stained with DAPI (blue). Scale bars 25 µm, in magnified panel 5 µm.

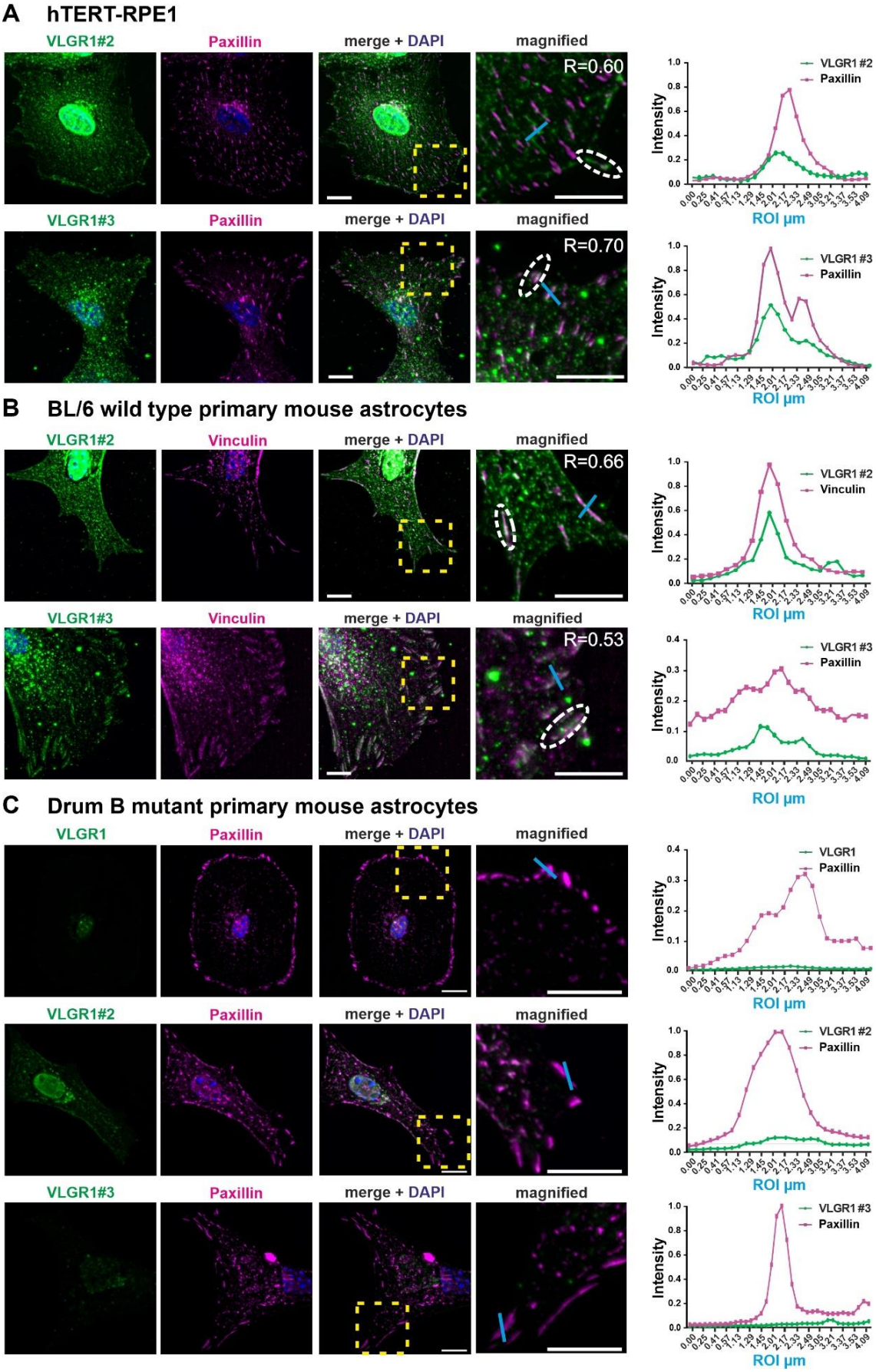
A
hTERT-RPE1
VLGR1#2
Paxillin
merge + DAPI
magnified
R=0.60
VLGR1#3
Paxillin
merge + DAPI
magnified
R=0.70
B
BL/6 wild type primary mouse astrocytes
VLGR1#2
Vinculin
merge + DAPI
magnified
R=0.66
VLGR1#3
Vinculin
merge + DAPI
magnified
R=0.53
C
Drum B mutant primary mouse astrocytes
VLGR1
Paxillin
merge + DAPI
magnified
VLGR1#2
Paxillin
merge + DAPI
magnified
VLGR1#3
Paxillin
merge + DAPI
magnified
Intensity
ROI µm
VLGR1 #2
Paxillin
VLGR1 #3
Paxillin
VLGR1 #2
Vinculin
VLGR1 #3
Paxillin
VLGR1
Paxillin
VLGR1 #2
Paxillin
VLGR1 #3
Paxillin

Figure S3. VLGR1 localization in FAs confirmed by immunostaining with alternative antibodies against VLGR1, Related to Figure 2. Immunofluorescence double labeling of paxilin or vinculin, respectively, (magenta) and of VLGR1 (green) by either the C-terminal pAb VLGR1#2 or the EAR-domain pAb VLGR1#3 in hTERT-RPE1 (A) and in primary BL/6 wildtype mouse astrocytes (B) reveal localization of VLGR1 in FAs confirming the data obtained by the C-terminal pAb VLGR1 used as standard antibody in the present paper. Positive Pearson correlation coefficient R calculated in magnified images for white dotted region indicates the degree of co-localization. Normalized fluorescence intensity plots (right hand) of VLGR1 and FA markers paxillin and vinculin, respectively share common peaks along the depicted blue line (ROI) in the magnified images indicating co-localization VLGR1 with both proteins in FAs. (C) Immunofluorescence double labeling of paxilin (magenta) and of VLGR1 (green) by either one of the three alternative antibodies used in the present study, namely VLGR1, VLGR1#2, and VLGR1#3 in primary astrocytes of VLGR1 deficient *Drum B* mice. In the absence of VLGR1 expression, all three VLGR1 antibodies do not stain FAs labeled with antibodies to paxilin, as confirmed by the normalized fluorescent intensity plots of ROIs indicated by blue lines. This demonstrates that all three antibodies specifically stain VLGR1 in FA when expressed (Fig. S1, and Fig. S3B). It is noted that the antibody staining in the nucleus, which is most pronounced by VLGR1#2 (see A and B), is reduced but not completely abolished in all three antibodies, indicating possible cross-reactivity with nuclear components.

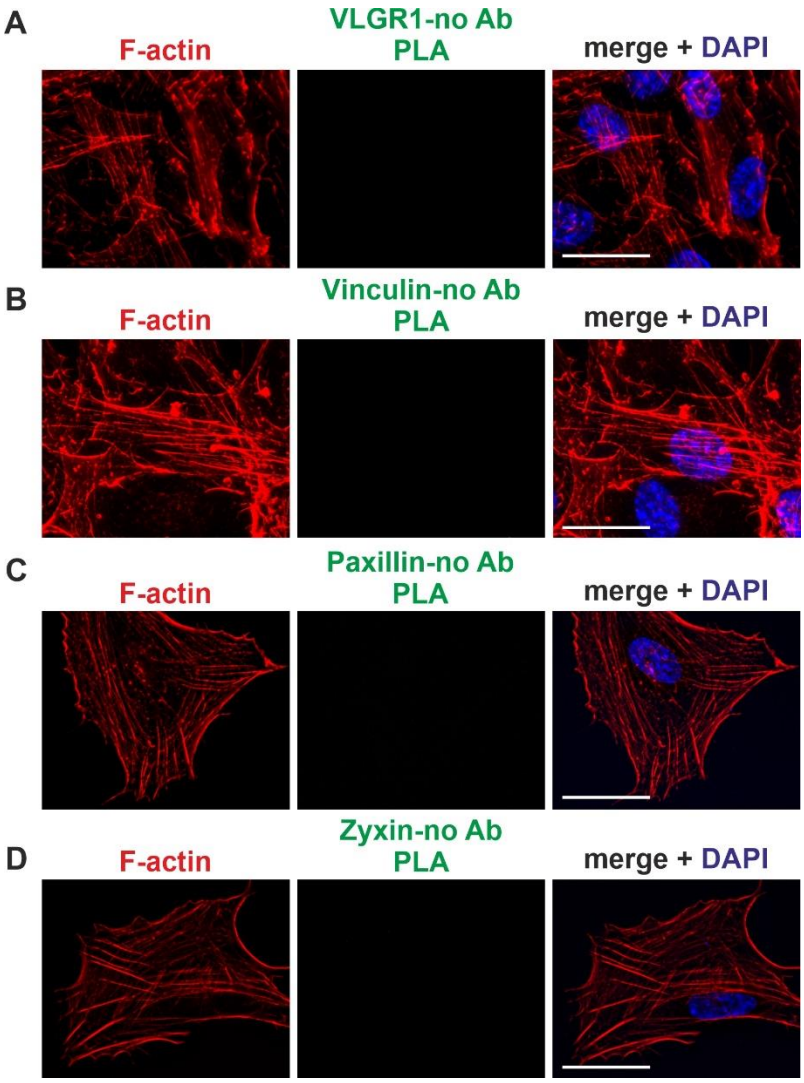

Figure S4. Controls of PLAs confirmed absence of false positive results in hTERT-RPE1 cells, Related to Figure 2. (A-D) In negative antibody controls, no PLA events could be detected (absence of green dots in second panel). TRITC-phalloidin (red) staining F-actin was used to visualize cell area, and nuclear DNA was stained with DAPI (blue). Scale bars, 25 µm.

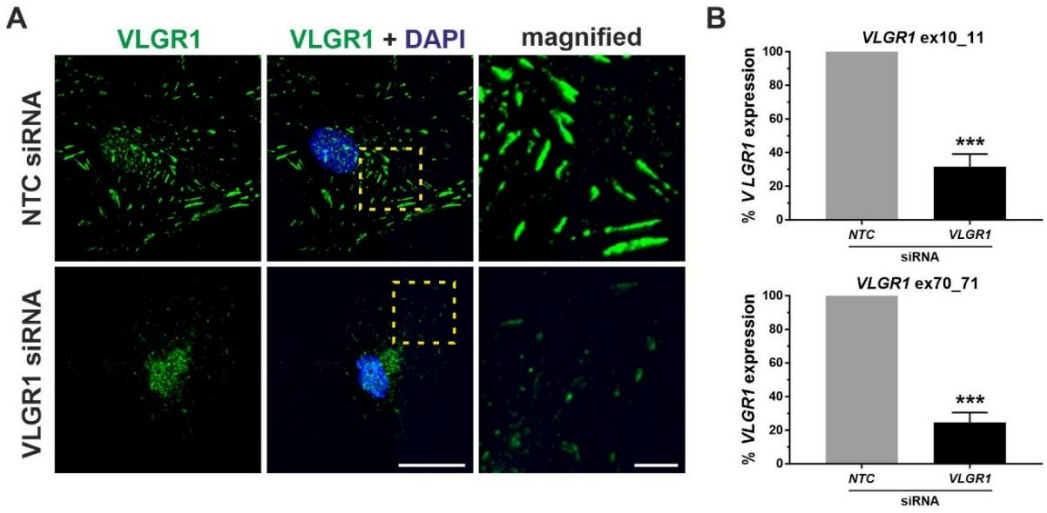

Figure S5. Validation of siRNAs for human VLGR1, Related to Figure 3. A) hTERT-RPE1 cells were transfected with a non-targeting control siRNA (NTC siRNA) or siRNA targeting *VLGR1* (*VLGR1* siRNA). 40 h after siRNA transfection, cells were fixed and immunostained for VLGR1 (green) to validate the knockdown efficacy. DAPI counterstaining in blue. (**B**) hTERT-RPE1 cells were lysed 48 h after siRNA transfection, and mRNA was extracted followed by qRT–PCR using primer sets specific to exon 10-11 and 70-71 of human *VLGR1*. *GAPDH* was used as reference. Graph shows expression levels of *VLGR1* in the knock down cells compared to that of corresponding NCT cells. Error bars show mean ± SD, three independent experiments. Statistical analyses were done using unpaired two-tailed t test.***P < 0.001.

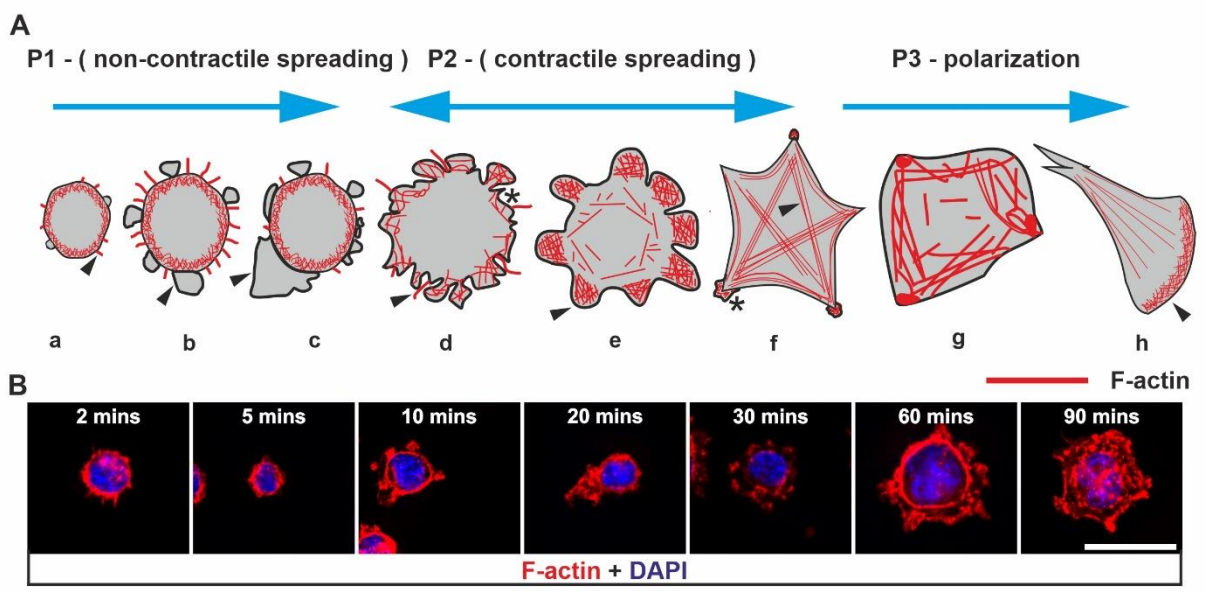

Figure S6. Phases of cell spreading, Related to Figure 4. A) Schematic representation of different phases of cell spreading phases introduced by Gauthier et al. (2012) and Greiner et al. (2013). (a) After seeding cells attach weakly to the substratum and are often rounded with very few thin F-actin microspikes emerging out (*arrow head*). (b) Cells start to spread, small membrane blebs (*arrow head*) and slightly longer microspikes are observed. (c) Thin layer of membrane starts stretching out from one side of the cell (*arrow head*) and the cell reaches its maximum adhesive area. (d) The cell progresses towards contractile spreading (P2) with alternate protrusions and retraction observed along the cell edge; occasional F-actin spikes are observed. (e) Membrane ruffles starts emerging from the edges of the cells. Stable FAs formation leads to homogenous protrusions and flower like cells are observed (*arrow head*). Cell exerts stronger forces and spreads further resulting in increased membrane area. (f) The cell experiences a drastic decrease in the membrane protrusions. Actin stress bundles (*arrow head*) become more prominent, membrane ruffles starts spreading along the edges and somewhat star-shaped cells are observed (*asterisk*). Cells start to polarize. (g) Cells protrude from one end maintaining constant membrane area. (h) Membrane protrudes towards one side forming lamellipodia (*arrowhead*) and at the rare end of the cell shrinks. The cell experiences high tension, which enables the cell to polarize. (B) HEK293T cells at different stages during cell spreading. Cells seeded on coverslips were stained for F-actin (red) after 2, 5, 10, 20, 30, 60 and 90 min to determine phases of cell spreading. DAPI (blue): nuclear DNA.

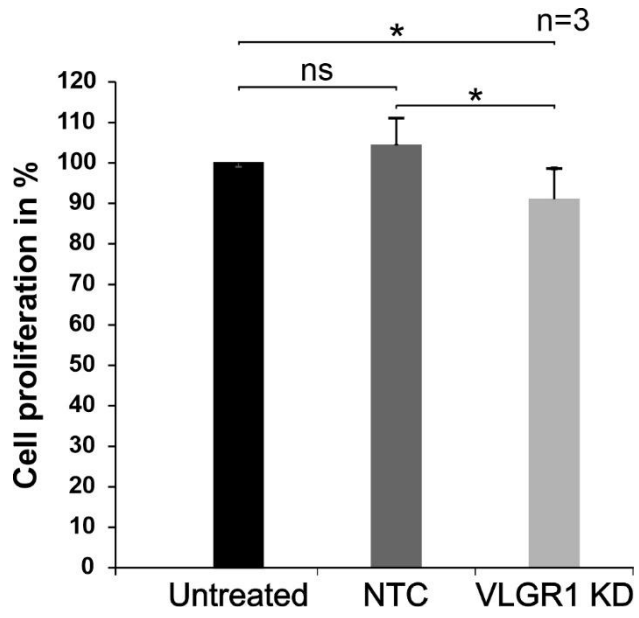

Figure S7. VLGR1 depletion affects proliferation of hTERT-RPE1 cells, Related to Figure 6. Quantification of three independent WST-1 proliferation assays revealed slightly reduced cell proliferation after siRNA-mediated VLGR1 knockdown when compared to untreated and non-targeting control (NTC) siRNA application, Data are represented as mean ± SD. Two-tailed Student's t test was applied, $*p < 0.05$, $**p < 0.01$, $***p < 0.001$.

Table S3. FA proteins identified in VLGR1 TAPs from hTERT-RPE1 cells, Related to Figure 1.

Gene name	Common protein name	Functional category
ACTN1	Alpha-actinin-1	*Actin regulation*
CFL1	Cofilin-1	*Actin regulation*
DPYSL2	Dihydropyrimidinase-like 2	*Actin regulation*
FLNC	Filamin-C	*Actin regulation*
MARCKS	Myristoylated alanine-rich C-kinase substrate	*Actin regulation*
MYH9	Myosin-9	*Actin regulation*
PTPN1	Protein tyrosine phosphatase 1B	*Actin regulation*
CAV1	Caveolin-1	*Adaptor/Cytoskeletal*
EZR	Ezrin	*Adaptor/Cytoskeletal*
GNB2L1	RACK1	*Adaptor/Cytoskeletal*
HAX1	HS1BP1	*Adaptor/Cytoskeletal*
TUBA1B	Tubulin	*Adaptor/Cytoskeletal*
VCL	Vinculin	*Adaptor/Cytoskeletal*
CALR	Calreticulin	*Chaperone*
CANX	Calnexin	*Chaperone*
HSPA2	HSP72	*Chaperone*
HSPB1	Heat shock protein beta-1	*Chaperone*
ITGB1	Integrin beta-1	*Adhesion receptor*
ITGA3	Integrin alpha-3	*Adhesion receptor*
SLC3A2	CD98	*Adhesion receptor*
CAD	Carbamoyl-phosphate synthetase 2	*Enzymes and protease*
MMP14	Matrix metalloproteinase-14	*Enzymes and protease*
PTPN1	Protein tyrosine phosphatase 1B	*Enzymes and protease*
HNRNPK	Heterogeneous nuclear ribonucleoprotein K	*RNA Metabolism*
RPL10L	Ribosomal protein L10-like;ribosomal protein 10	*RNA Metabolism*
SLC16A3	MCT4	*Channel*

Transparent Methods

Animals

All experiments described herein were performed in accordance with guidelines provided by Association for Research in Vision and Ophthalmology. *Vlgr1*-del7TM leads to the deletion of the entire 7TM domain of *Vlgr1* (McMillan and White, 2004). *Drum B* mice were identified in an ENU (N-ethyl-N-nitrosourea) mutagenesis screen (Potter et al., 2016). The c.8554+2t>c mutation the donor splice site of exon 37 resulting in a premature stop Codon in intron 37-38. Both mouse lines are bread on a C57BL/6 background.

Antibodies and dyes

Antibodies used are directed to vinculin (Merck, Darmstadt, Germany), paxillin (Abcam, Cambridge, United Kingdom), zyxin (Abcam, Cambridge, United Kingdom), FAK and pFAK397 (CST, Frankfurt, Germany). In most experiments we applied a rabbit poyclonal antibody (pAb) against the C-terminus of murine VLGR1 (aa 6198 – 6307) previously characterized in our lab (Maerker et al., 2008). We confirmed the localization of VLGR1 in FAs by using two alternative rabbit pAbs: VLGR1#2 against the C-terminus of murine VLGR1 (aa 6159–6306) and VLGR1#3 against an extracellular region of murine VLGR1 bodies against (amino acids 3249 – 3425), both kindly provided by Dr Dominic Cosgrove, Omaha, USA) (MacGee et al., 2006; Maerker et al., 2008; Zallocchi et al., 2012). Secondary antibodies conjugated to Alexa488, Alexa555, Alexa568 or Alexa647 were purchased from Molecular Probes (Life Technologies, Darmstadt, Germany) or from Rockland Inc. (Gilbertsville, PA, USA). DNA was stained with 4',6-diamidino-2-phenylindole (DAPI, Merck). F-actin was labelled with TRITC-phalloidin (Merck).

Cell culture

hTERT-RPE1 and HEK293T cells were cultured in DMEM-F12 or DMEM (ThermoFisher Scientific, Darmstadt, Germany)/10% fetal bovine serum (FBS), and 1% penicillin/streptomycin (ThermoFisher Scientific). Mouse embryonic fibroblasts (MEFs) were cultured in DMEM/10% FBS and 1% penicillin/streptomycin. Primary astrocyte cultures were prepared from cerebral cortices of C57BL/6 WT, *Vlgr1*/del7TM or *Drum B* mutant postnatal stage day 1 (PN1) mice. Mouse cortices (6-10) were enzymatically dissociated with DNase/trypsin followed by mechanical dissociation. Single cells were cultured in DMEM/10% FBS/2 mM l-glutamine 1% penicillin/streptomycin and 50 µg/ml gentamycin. Medium was changed at days 1, 2 and 7 after plating. Upon confluence, oligodendrocytes were removed. After trypsinization and DNAse treatment of still attached cells, astrocytes were passed over successive Petri dishes to get rid of microglia. Astrocytes were maintained in complete media and used after 14 days culture.

siRNA transfection

ON-TARGETplus siRNA SMARTpools for non-targeting pool (D-001810-10-05) and the siRNAs targeting human *VLGR1* (ThermoFisher Scientific) were transfected using 20 nM siRNA with Lipofectamine RNAimax (ThermoFisher Scientific).

Tandem affinity purification (TAP) and mass spectrometry

TAP was performed as described previously (Knapp et al. 2019; Boldt et al. 2016). In brief, VLGR1 domains were tagged with the tandem Strep II/FLAG tandem affinity purification tag (SF-TAP) (Fig. 1A). SF-tagged VLGR1 versions were expressed in hTERT-RPE1 cells for 48 h lysed and cleared by centrifugation. Mock-treated hTERT-RPE1 cells were used as controls. Supernatant were then subjected to a two-step purification on Strep-Tactin® Superflow® beads (IBA, Goettingen, Germany) and anti-FLAG M2 agarose beads (Merck). Competitive elution was achieved by desbiothin (IBA) in the first step and FLAG® peptide (Merck), respectively. Eluates, precipitated by methanol-chloroform were subjected to liquid chromatography coupled with tandem mass spectrometry (LC-MS/MS) (Boldt et al. 2016). Raw spectra were searched against the human SwissProt database using Mascot and results were verified by Scaffold (version Scaffold 4.02.01, Proteome Software Inc.) to validate MS/MS-based peptide and protein identifications.

Data processing

TAP data was compared to the according data for mock-transfected cells. Proteins that occurred in the mock data set were not further considered. Datasets were also compared to common control TAPs of the RAF1-protein (Gloeckner et al., 2009, Boldt et al., 2016). Gene names of preys were used as input for the Cytoscape plugins STRING and ClueGO and the STRAP software. The parameter *confidence (score) cutout* was set to 0.4 and the parameter *maximum number of interactors* was set to 0 for STRING analysis. ClueGO v2.3.3 was used for Gene Ontology (GO) term enrichment analysis. Network specificity was set to default (medium).

Immunofluorescence

Cells were fixed with 2% paraformaldehyde, washed and incubated with 50 mM NH_4Cl for 10 min. Samples were permeabilized with PBSTX (0.2% Triton-X) and blocked with 0.1% ovalbumin, 0.5% fish gelatin in PBS before primary antibodies were incubated overnight at 4°C. After washing, samples were incubated with secondary antibodies and DAPI for 1 h. After washing, cover slips were mounted in Mowiol (Roth, Germany). Specimens were analyzed on a Leica DM6000B microscope (Leica, Bensheim, Germany), images were processed, deconvoluted and co-localization profiles generated with Leica and Fiji (https://fiji.sc) image analysis software.

Cell spreading assay

24 h post siRNA transfection, 1 x 10^5 cells/well were seeded in a 6-well plate on either poly-L-lysine or fibronectin (Merck) coated coverslips. Poly-L-lysine was used for adhesion and fibronectin to promote cell spreading. After indicated periods of replating, cells were fixed and immunofluorescence analysis was performed. The area of the cells was analyzed using Fiji image analysis software.

Morphometric analysis of FAs

For the FAs morphometric analysis, vinculin was used as a marker protein. The length and number of FAs were quantified applying a modified protocol (Horzum et al., 2014). FA image analysis was implemented using Fiji. Briefly, the images were processed with fast Fourier transformation followed by a band pass filter to normalize the background. The images were thresholded, converted to binary images and analyzed using the built-in 'analyze particles' macro in Fiji, where large is defined as 40 or more pixels. This automatically generated the number and morphometric details of the FAs. The length of FAs was manually determined using the line option tool in Fiji.

Cell migration assay

Collective cell migration assay (Rodriguez et al., 2005) was performed 48 h after siRNA transfections of hTERT-RPE1 cells and in *Vlgr1*-del7TM primary astrocytes. The scratch wound was made by cutting cell monolayer longitudinally with a 200-µl or a 10-µl pipette tip in hTERT-RPE1 cells and astrocytes, respectively. Cells were allowed to migrate into the "wound" for indicated time points, fixed and stained. Image analysis to calculate wound closure was performed using Fiji. For single-cell tracking *Vlgr1-del7TM* mutant and WT Bl/6 mouse primary astrocytes were seeded on fibronectin-coated chambers at low density. Live-cell imaging performed under 5% CO_2 and at 37°C using Nikon Eclipse Ti2-E equipped with a spinning disc. D.I.C. images were acquired using a 20x microscope objective every 15 minutes for 24 h for a total in 97 time points. Cells were tracked using a Fiji manual tracking plugin and plot data were generated using Chemotaxis and Migration Tool 2.0 (Ibidi, Munich, Germany).

Proximity ligation assay (PLA)

In situ PLA was used to visualize protein – protein interactions in hTERT-RPR1 cells using Duolink In Situ FarRed Kit Mouse/Rabbit (Merck) according to the manufacturer's instruction. Cells were incubated overnight at 4°C with primary anti-bodies followed by anti-rabbit PLUS and anti-mouse MINUS secondary PLA probes. The two complementary oligonucleotides were then hybridized, ligated and amplified by rolling circle amplification, resulting in fluorescence spots when the targeted proteins were closer than 30-40 nm.

Shear-stress experiments

For shear-stress experiments, 24 h post siRNA transfections cells were replated into µ-slides (Ibidi), cultured for 24 h, and subjected to static conditions or shear stress of 20 dyn/cm^2 for 20 min using the

Ibidi pump system. Afterwards, the cells were fixed, stained and analyzed using Leica TCS SP5 confocal laser-scanning microscope (Leica) and Fiji.

Western blot analysis

Protein lysates were prepared using RIPA lysis buffer (10 mM Tris, 1mM $CaCl_2$, 150 mM NaCl, 10 mM NaF, 20 mM ß-Glycerophosphate, 0.5% Nonident P-40, 0.5% Deoxycholic acid, 0.1% SDS, pH 7.4) containing complete protease inhibitor cocktail (04693132001, Roche Diagnostics, Mannheim, Germany) and sonicated. Protein content was quantified using the BCA protein assay (Merck) and subjected to SDS-PAGE. After blotting, the polyvinylidene difluoride membranes (PVDF FL) (Millipore, Schwalbach, Germany) were blocked in AppliChem blocking reagent (AppliChem, Darmstadt, Germany) for 1 h. The membranes were incubated with primary antibodies overnight followed by appropriate secondary antibodies Alexa Flour 680 (Invitrogen) or IR Dye 800 (Rockland, Gilbertsville, USA). Scans of the blot were made employing the Odyssey infrared imaging system (LI-COR Biosciences, Bad Homburg, Germany). For densitometry analysis Fiji was used.

Quantitative Real-time PCR (qRT-PCR)

RNA from control and *VLGR1*-deficient RPE1 cells was isolated using TRIzol (ThermoFisher Scientific). 4 µg RNA was reverse transcribed to cDNA using the SuperScript III first-strand synthesis system. qRT-PCR was performed using the Platinum™ SYBR™ Green qPCR SuperMix-UDG (ThermoFisher Scientific) with the Applied Biosystems® 7500 Real-Time PCR System. The relative expression levels of the target genes were normalized *GAPDH*. Primer pairs used: *VLGR1*,
forward: 5′-CAGCCGATTGTTACCGAAAATG-3′,
reverse: 5′- AGCATCACAGTCACCAGTTG -3′;
and *GAPDH*,
forward primer: 5′-GAGGTCAAGGGATTTGGTCGT-3′,
reverse primer: 5′−TTGATTTTGGAGGGATCTCG-3′.

Statistical analyses

Statistical analyses were performed using Graphpad Prism 7.0 software (GraphPad Software Inc., San Diego, CA, USA). Differences between two groups were compared using two-tailed Student's t test. For multiple group comparisons, ANOVA followed by Dunnett's multiple comparison tests and Sidak's multiple comparison tests were performed depending on the data to be compared. Differences were considered significant at *$p < 0.05$, ** $p < 0.01$, ***$p < 0.001$. Bar plots are presented as mean ± SD. Box plots show median (middle line), edge of boxes is top and bottom quartiles (25–75%), and whiskers represent the ranges for the upper 25% and the bottom 25% of data values.

WST-1 cell proliferation assay

The cell proliferation of hTERT-RPE1 cells was tested by using the WST-1 cell proliferation assay (Roche Diagnostics). hTERT-RPE1 cells were seeded on 96 well plate at a density of $4x10^3$ cells per well as described in the manufacturer's protocol (Roche Diagnostics). After 24 h cells were treated with VLGR1 siRNA and non-targeting (NTC) siRNA for 48 h. Subsequently, 10 µl WST-1 tetrazolium salt (4-[3-(4-Iodophenyl)-2-(4-nitro-phenyl)-2H-5-tetrazolio]-1,3-benzene sulfonate) were added into wells which contain 100 µl growth medium and cells were incubated at 37°C with 5% CO_2 for 4 h. Absorbance values at 460 nm were measured using a Vario Skan Flash (ThermoFisher Scientific) plate reader. Averages of spectrophotometric absorbance values were calculated and blank control value was subtracted.

Supplemental references

Horzum, U., Ozdil, B. & Pesen-Okvur, D. 2014. Step-by-step quantitative analysis of focal adhesions. MethodsX*,* 1**,** 56-9.

Potter, P. K., Bowl, M. R., Jeyarajan, P., Wisby, L., Blease, A., Goldsworthy, M. E., Simon, M. M., Greenaway, S., Michel, V., Barnard, A., Aguilar, C., Agnew, T., Banks, G., Blake, A., Chessum, L., Dorning, J., Falcone, S., Goosey, L., Harris, S., Haynes, A., Heise, I., Hillier, R., Hough, T., Hoslin, A., Hutchison, M., King, R., Kumar, S., Lad, H. V., Law, G., Maclaren, R. E., Morse, S., Nicol, T., Parker, A., Pickford, K., Sethi, S., Starbuck, B., Stelma, F., Cheeseman, M., Cross, S. H., Foster, R. G., Jackson, I. J., Peirson, S. N., Thakker, R. V., Vincent, T., Scudamore, C., Wells, S., El-Amraoui, A., Petit, C., Acevedo-Arozena, A., Nolan, P. M., Cox, R., Mallon, A. M. & Brown, S. D. 2016. Novel gene function revealed by mouse mutagenesis screens for models of age-related disease. Nat Commun*,* 7**,** 12444.

Rodriguez, L. G., Wu, X. & Guan, J. L. 2005. Wound-healing assay. Methods Mol Biol*,* 294**,** 23-9.

Zallocchi, M., Delimont, D., Meehan, D. T. & Cosgrove, D. 2012. Regulated vesicular trafficking of specific PCDH15 and VLGR1 variants in auditory hair cells. J Neurosci*,* 32**,** 13841-59.